



# Characterization of benzoxazine resins for brake pad friction materials manufacturing

Davide Carlevaris<sup>1</sup> · Cinzia Menapace<sup>1</sup> · Giovanni Straffelini<sup>1</sup> · Luca Fambri<sup>1</sup>

Received: 15 June 2022 / Accepted: 6 November 2022  
© The Author(s) 2022

## Abstract

Phenolic resins are the most commonly used binders in brake pads for automotive disc brake systems owing to their affordability and thermal properties. However, they also show some limitations related to their crosslinking mechanism. Benzoxazine resins present themselves as possible alternatives for this application by providing enhanced thermal properties as well as other industrially attractive characteristics such as lower moisture absorption and unlimited shelf life. This study investigates the thermal properties of two different benzoxazine resins, with the aim of assessing their capabilities as binder for brake pad and of understanding how to process them in order to actually employ them as such. DSC, TGA, hardness and tribological analyses were carried out on neat resin samples and on friction materials containing them as binder. The presence of several concurring reactions was detected during the crosslinking reaction of benzoxazine resins. The benzoxazine resins showed lower mass loss respect to a phenolic resin in the temperature range of interest for commercial brake pads application. Friction material containing benzoxazine resin binder showed promising tribological results.

**Keywords** Benzoxazine resins · Curing · Brake pads · Thermal degradation

## Abbreviations

BA-a	Benzoxazine resin monomer based on bis-phenol A and aniline
BF-a	Benzoxazine resin monomer based on bis-phenol F and aniline
R6	Benzoxazine resin based on BA-a
R7	Benzoxazine resin based on BF-a
Ph	Commercial phenolic resin
R6_fm	Friction material adopting R6 as binder
R7_fm	Friction material adopting R7 as binder
Ph_fm	Friction material adopting Ph as binder
DSC	Differential scanning calorimetry
STA	Simultaneous thermal analysis
TGA	Thermogravimetric analysis

DTG	Differential thermogravimetric analysis
$\mu$	Coefficient of friction, dimensionless
COF	Coefficient of friction, dimensionless
Ka	Specific wear coefficient, $10^{-14} \text{ m}^2 \text{ N}^{-1}$
$T_g$	Glass transition temperature, °C
$T_{\text{peak}}$	Temperature of exothermic peak, °C
$E_a$	Activation energy, $\text{kJ mol}^{-1}$
$\alpha$	Conversion rate of the reaction, dimensionless
$\varphi$	Heating rate, $^{\circ}\text{C min}^{-1}$
$m_{\text{LOSS},250^{\circ}\text{C}}$	Mass loss at 250 °C, %
$m_{\text{LOSS},650^{\circ}\text{C}}$	Mass loss at 650 °C, %
$T_{\text{MLR}}$	Temperature of maximum mass loss rate, °C
$\rho$	Density, $\text{g cm}^{-3}$

✉ Cinzia Menapace  
cinzia.menapace@unitn.it

Davide Carlevaris  
davide.carlevaris@unitn.it

Giovanni Straffelini  
giovanni.straffelini@unitn.it

Luca Fambri  
luca.fambri@unitn.it

<sup>1</sup> Department of Industrial Engineering, University of Trento, Via Sommarive 9, 38123 Trento, Italy

## Introduction

Disc brake systems are the most established braking system in the automotive field. Their working principle consists in the dissipation of kinetic energy into heat by friction, thus implying a temperature increase of the braking system itself. They comprise a cast iron rotor, the disc and a friction material lining, also known as brake pad. Brake pad materials include a multitude of ingredients, which easily exceed the

dozens [1], but can be broadly divided into four categories: reinforcing materials, friction modifiers, fillers and binders.

The binder constitutes the matrix of the friction material composite and is therefore responsible for its structural integrity. In the case of conventional automotive applications, i.e. light-duty vehicles (but also trucks), the most used binders are phenolic resins [2] due to their advantageous cost and satisfactory thermal properties. The latter are of paramount importance in brake system applications because the increase in brake pad temperature during operation may lead to the degradation of the binder and consequently to higher wear [3, 4], and, over a certain threshold temperature, to a sharp increase in the emission of sub-micrometric particulate matter (PM<sub>1</sub>) [4–7]. However, phenolic resins show some limitations given by the shrinkage during curing accompanied by gaseous species evolution, which can influence the structural integrity of the composite product, and by their limited shelf life [8, 9], which is mostly related to moisture susceptibility. Industrially, friction materials for brake pads are cured in ovens either in batch or following a continuous process [10]. Currently, convective ovens are the most widespread equipment, but IR ovens, providing more efficient heating through irradiation, are becoming more popular [10].

A relatively new class of resins, called *polybenzoxazines* or *benzoxazine resins*, offers attractive properties for binder applications. These resins have been first synthesized in 1944 by Holly and Cope [11] but have gained industrial interest only in the last couple of decades, owing to their good mechanical and thermal properties [12–15], which make them solid candidates as brake pad binders. Furthermore, these resins show some other interesting properties, such as dimensional stability and low byproduct formation upon curing, low moisture absorption and unlimited shelf life [16–18]. The crosslinking mechanism of benzoxazine resins, which consists in an addition polymerization known as ring-opening polymerization [19–21], allows for the unlimited shelf life and for the minimal volumetric change and evolution of byproducts during curing, as opposed to the condensation polymerization process of phenolic resins. The ring-opening polymerization of benzoxazine resins is a thermally activated process. Therefore, the conventional curing process for these resins only consists of a heat treatment. However, innovative processes such as high-pressure curing were shown to be able to affect the properties of certain types of resins [22]. Additionally, acid and/or basic catalysts can be adopted to improve the processing window and the final properties of benzoxazine resins [23]. Benzoxazine resins also show some particularly developed inter- and especially intra-molecular hydrogen bonding, which bestow unexpectedly good mechanical properties and moisture resistance to the crosslinked material [14, 17, 20, 24]. Furthermore, the chemical structure of benzoxazine resins

is highly customizable [25–27], allowing for the possibility to tune some of their properties according to the desired application.

Although benzoxazine resins show attractive characteristics, both in terms of industrial management and thermal properties, there are several possible chemical bonds that can form upon crosslinking [24, 28] and that are responsible for the actual properties of the final product. The “phenolic Mannich bridge” structure is believed to be the main bond formed during curing, but it is not the most stable between the possible obtainable structures [24, 28]. The type of bonding chemical structure, which determines the properties of the final product, is influenced by the structure of the uncured resin monomer [24, 26] and also by the adopted curing thermal process [29]. Furthermore, it has been shown that a binder resin might behave differently when processed together with the other ingredients in a composite material, also in the specific case of a friction material mixture [30–33].

Gurunath et al. [34] studied the possible application of benzoxazine resins in friction materials. Although their results were promising, they did not take into account the wear of the brake linings, which is arguably one of the parameters most influenced by the binder, and did not provide any insight respect to how the resins are affected by the curing process. Furthermore, the types of utilized benzoxazine resin monomers were not specified.

In this study, the curing mechanism and the thermal stability of some benzoxazine resins were analysed as both neat resins and in a friction material mixture, in order to assess the feasibility of their application as a binder for brake pads. Friction materials prepared with benzoxazine resins binder were subjected to tribological testing to evaluate their braking capabilities and wear behavior. As previously mentioned, benzoxazine resins possess attractive properties from an industrial standpoint. Their thermal properties could improve wear and emissions of the brake pads, and their shelf life would ease its transportation and storage management and costs. With this work, we aim to provide an improved characterization of benzoxazine resins in friction materials, as well as of the friction materials containing them, which could provide solid bases for a future industrial application.

## Materials and methods

### Materials

Two different benzoxazine resins, hereby referred to as “R6” and “R7”, were supplied by Huntsman International LLC. These resins are, respectively, based on BA-a and BF-a monomers, shown in Fig. 1, which are formally derived

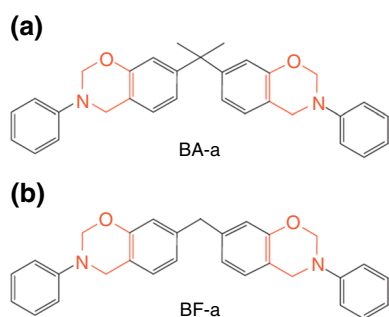


**Fig. 1** Benzoxazine resin monomers of (a) BA-a and (b) BF-a

from bisphenol A and bisphenol F, and are the simplest and cheapest form of multifunctional benzoxazine monomers. Brembo S.p.A. supplied a commercial phenolic resin binder in powder form, referred to as “Ph”, and a reference commercial friction material mixture that did not include any binder. The reference friction material therefore comprised all the reinforcing components, friction modifiers (such as abrasives and lubricants) and fillers in the fractions employed in the original commercial composition. Grey cast iron discs having a diameter of 60 mm and a hardness of 258 HV10, directly cut from car disc brakes, were supplied by Brembo S.p.A.

### Sample preparation

Phenolic resin was supplied directly in powder form, while R6 and R7 were supplied in a glassy block form. Pieces extracted from the solid blocks were therefore pulverized with a Fritsch Analysette 3 vibration mill using a WC sphere for easier handling and dosing.

Benzoxazine resin disc samples were produced by curing approximately 10 g of R6 and R7 inside aluminium-wrapped cups using a muffle furnace controlled by a Fuji Electric PXR4 temperature controller. The curing procedure suggested by the supplier consisted in:

- 5 °C min<sup>-1</sup> heating to 130 °C, followed by a 1.3 °C min<sup>-1</sup> heating to 150 °C and a final 0.4 °C min<sup>-1</sup> heating to the maximum temperature of 200 °C, maintained for 1 h.

The discs were then extracted by peeling off the surrounding aluminium foil. An example of the effect of the curing process performed on a benzoxazine resin is presented in Fig. 2.

Three different friction materials were produced by mixing 7% by mass of R6, R7 and phenolic resin to the commercial friction material mixture. The three batches were blended by a WAB T2F turbula mixer for 15 min to ensure a homogeneous distribution of the ingredients. Cylindrical friction material samples, with a diameter of 10 mm, were

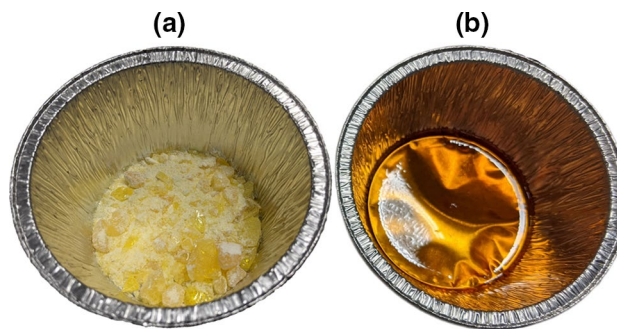


**Fig. 2** Effect of the curing process on R7 benzoxazine resin. Solid pieces and powder of unreacted R7 monomer (a) become a solid homogeneous disc after thermal treatment (b)

then produced for each of the three friction material mixtures by hot moulding and curing. Hot moulding of the samples was performed at 150 °C for 10 min applying 100 MPa of pressure using a Buehler Pneumat I mounting press. Two different curing processes, schematized in Fig. 3, were used depending on the type of binder. In case of phenolic resin, the multistep curing procedure consisted in:

- 5 °C min<sup>-1</sup> heating to 70 °C, followed by a 1 °C min<sup>-1</sup> heating to 80 °C maintained for 45 min, followed by a 2 °C min<sup>-1</sup> heating to 100 °C maintained for 45 min, and a final 1.3 °C min<sup>-1</sup> heating to 180 °C for 1 h. This curing thermal treatment is schematized in Fig. 3a.

In the benzoxazine resin case, the multistep curing mimicked the one used for neat resins:

- 5 °C min<sup>-1</sup> heating to 130 °C, followed by a 1.3 °C min<sup>-1</sup> heating to 150 °C and a final 0.4 °C min<sup>-1</sup> heating to 200 °C maintained for 1 h. This curing thermal treatment is schematized in Fig. 3b.

All curing processes were performed in an aerated muffle furnace. Free cooling inside the furnace followed the thermal treatments. The friction material pins were named R6\_fm, R7\_fm, and Ph\_fm, respectively, referring to the R6, R7 and phenolic-containing samples. A block diagram schematizing the steps of the friction materials preparation process is shown in Fig. 4.

## Experimental techniques

### Thermal analysis

Differential scanning calorimetry (DSC) was performed by means of a Mettler DSC-30 power compensation calorimeter to investigate the crosslinking reaction of the resins. Samples of R6 and R7 were tested at four different heating

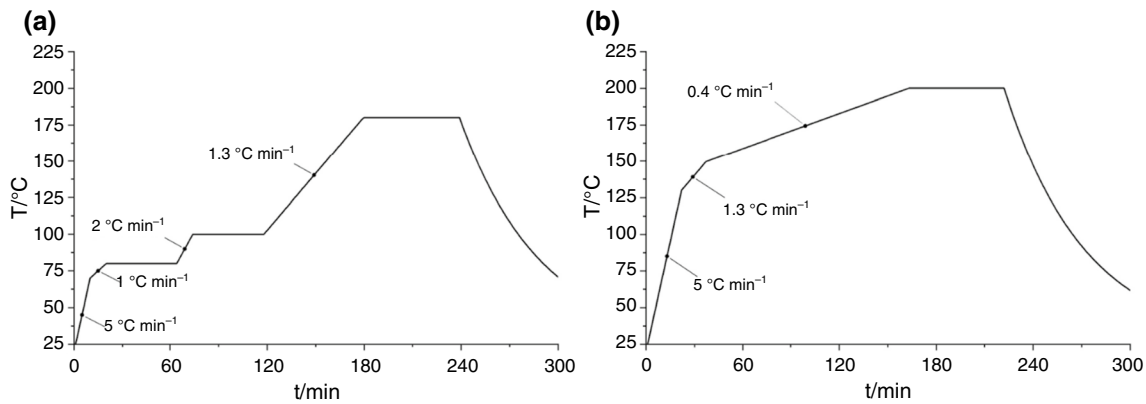


**Fig. 3** Time–temperature curves of the curing thermal treatments performed on Ph (a) and on R6 and R7 benzoxazine resins (b)

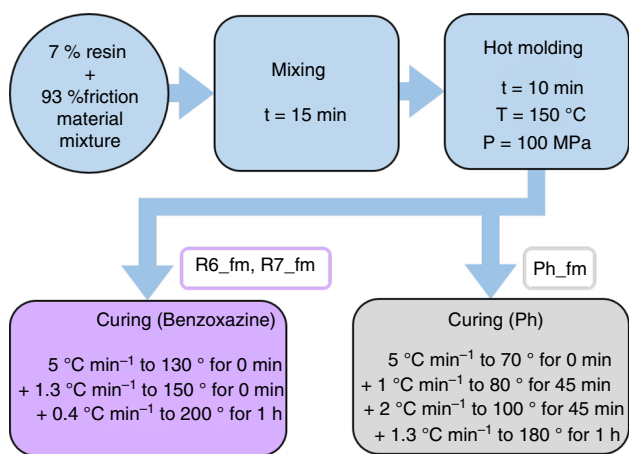


**Fig. 4** Schematic representation of the procedure adopted for the production of the friction material samples R6\_fm, R7\_fm and Ph\_fm

rates (10, 3, 1 and 0.3 °C min<sup>-1</sup>) up to 270 °C under nitrogen atmosphere provided through a 100 ml min<sup>-1</sup> N<sub>2</sub> flux. Following ASTM E1356, a further DSC scan at 10 °C min<sup>-1</sup> was performed after each DSC analysis in order to measure the glass transition temperature ( $T_g$ ) of the reacted resins.

A Kissinger–Akahira–Sunose analysis was performed on the data to determine the activation energy of the crosslinking process of the benzoxazine resins for different conversion percentages, and thus different curing degrees, of the reactions.

Phenolic resin was tested under the same conditions, but only a single DSC test with a 10 °C min<sup>-1</sup> heating rate was ran. R6 and R7 underwent further DSC-TGA testing at 10 °C min<sup>-1</sup> up to 300 °C under air atmosphere using a Netzsch STA 409 Luxx thermal analyser.

In order to investigate the production process of benzoxazine resin-bound friction materials, the results of these first tests were used to determine some preliminary partial heat treatments, representative of the curing steps adopted

for the benzoxazine resins. The effects of these curing steps were then evaluated by performing a DSC analysis, with the same aforementioned parameters, on both R6 and R7. Three preliminary curing steps were determined: a first one at 145 °C for 3 h, a second one at 170 °C for 2 h, and a third one at 190 °C for 2 h. These curing cycles will be, respectively, referred to as “145/3 h”, “145 + 170” and “145 + 190”. While the first step was performed on the initial resin powders, both the second and third steps were carried out on fragments obtained after the first curing step at 145 °C. All these heat treatments were conducted in a muffle furnace with a heating rate of 5 °C min<sup>-1</sup>. The results of these tests are reported in the “Appendix A2” section of the paper.

Thermogravimetric analyses (TGA) were performed using a Netzsch STA 409 Luxx thermal analyser in order to investigate the degradation temperatures of the resins. Samples of approximately 25 mg of phenolic and benzoxazine resin underwent testing with a heating rate of 10 °C min<sup>-1</sup> up to 1050 °C. These analyses were performed under air and under nitrogen flux. Air simulates the brake pads working conditions, while N<sub>2</sub> is used to test the resin under an inert atmosphere.

Samples of friction materials (R6\_fm, R7\_fm and Ph\_fm) underwent thermogravimetric analysis under the same conditions, but only an air flux was employed for these tests.

### Hardness analysis

Shore D hardness testing was performed with a Hildebrand Shore D hardness tester. R6 and R7 benzoxazine resin discs, R6\_fm, R7\_fm and Ph\_fm friction material samples underwent Shore D testing following ASTM D2240. The hardness of the friction materials was also tested on the surface that underwent tribological testing.

## Tribological analysis

Tribological analysis was performed using a Ducom DHM-600 Pin-on-Disc tribometer. Cylindrical pin samples with a 10 mm diameter of R6\_fm, R7\_fm and Ph\_fm were tested for 90 min at a constant sliding speed of  $1.51 \text{ m s}^{-1}$  (at the centre of the pin) under a load of 79 N, which results in roughly 1 MPa of nominal contact pressure. The sliding counterface consisted in grey pearlitic cast iron discs, which is the most commonly used material for car brake discs. Before testing, all pins underwent a run-in stage under the same testing parameters, which lasted at least 30 min or until the surface of the samples achieved complete contact (*macroscopically conformal contact*) with the counterface disc.

During the test, the temperature and the coefficient of friction were recorded. The friction coefficient  $\mu$  (or “COF”) is the coefficient through which the force applied perpendicularly to the moving mating surfaces  $F_N$  is converted into a tangential force  $F_t$  known as “frictional force”, following Eq. (1):

$$F_t = \mu \cdot F_N \quad (1)$$

The specific wear coefficient of the pin “Ka” was also calculated according to Eq. (2):

$$Ka = \frac{V_w}{F_N \cdot s} \quad (2)$$

where  $V_w$  is the wear volume,  $F_N$  is the normal applied force, and  $s$  is the sliding distance.

## Results and discussion

### Differential scanning calorimetry

#### Neat resins DSC results

Preliminary  $10 \text{ }^\circ\text{C min}^{-1}$  DSC analyses were performed on R6, R7 and Ph samples to compare how the reaction temperature range of the investigated resins is positioned respect to the processing window commonly utilized in the preparation of friction materials by hot moulding and curing steps [35–37]. The resulting area-normalized DSC curves are reported in Fig. 5 together with the processing temperature window. While the exothermic peak of Ph resin is located below the hot moulding temperature, those of R6 and R7 appear above the highest temperature commonly reached during processing. Therefore, further analyses were necessary in order to tailor the processing parameters for the benzoxazine resins.

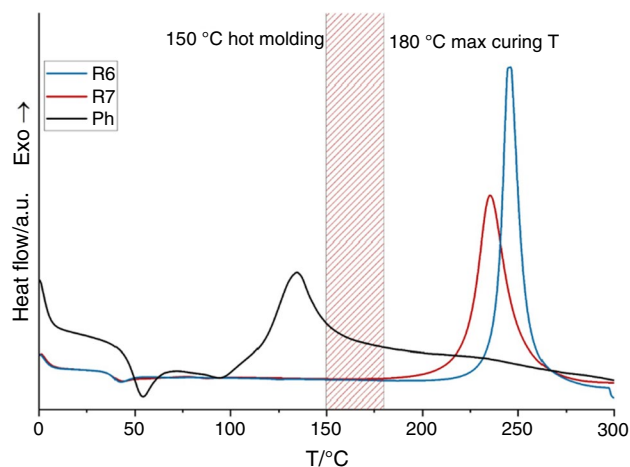


**Fig. 5**  $10 \text{ }^\circ\text{C min}^{-1}$  area-normalized DSC curves of R6, R7 and Ph resins. The dashed area indicates the commonly used processing temperature interval

Figure 6 shows the DSC curves of R6 and R7 obtained at 10, 3, 1 and  $0.3 \text{ }^\circ\text{C min}^{-1}$  heating rates in  $\text{N}_2$  atmosphere. All curves show a clear exothermic peak, which represents the crosslinking reaction evolution. The R7 peaks are smaller in height and appear at lower temperatures respect to the R6 peaks for every heating rate.

The curves shown in Fig. 6 are rearranged in Fig. 7, showing an area-normalized peak comparison between the different heating rates for both R6 and R7 benzoxazine resins. These graphs clearly illustrate how lowering the heating rate of the DSC analyses results in the shifting of the observed reactions, both of their onset and their peak, to lower temperatures, which is a well-known phenomenon [28, 38].

The peak temperature, the crosslinking energy, and the post-DSC glass transition temperature ( $T_g$ ) of the benzoxazine resins, obtained from the DSC analyses, are listed in Table 1. The crosslinking energy was calculated as the area of the power-time DSC curve. The  $T_g$  values were obtained by applying the tangent method, following ASTM E1356, to a second DSC scan performed at  $10 \text{ }^\circ\text{C min}^{-1}$  immediately after each test. Therefore, the glass transition temperature values listed in Table 1 are properties of the resins cured with different heating rates, and are not related to the inflection points visible at the beginning (below  $50 \text{ }^\circ\text{C}$ ) of the curves shown in Figs. 6 and 7, which would instead refer to the  $T_g$  of the unreacted resin monomers. The peak temperatures are higher for the R6 resin, and both resins see similar drop in the  $T_{\text{peak}}$  values by lowering the heating rate, in agreement with the observations made concerning data reported in Fig. 6. The crosslinking energy values of R6 and R7 do not show a clear influence of the heating rate. Moreover, these values vary in a short range in the case of R6, while in the R7

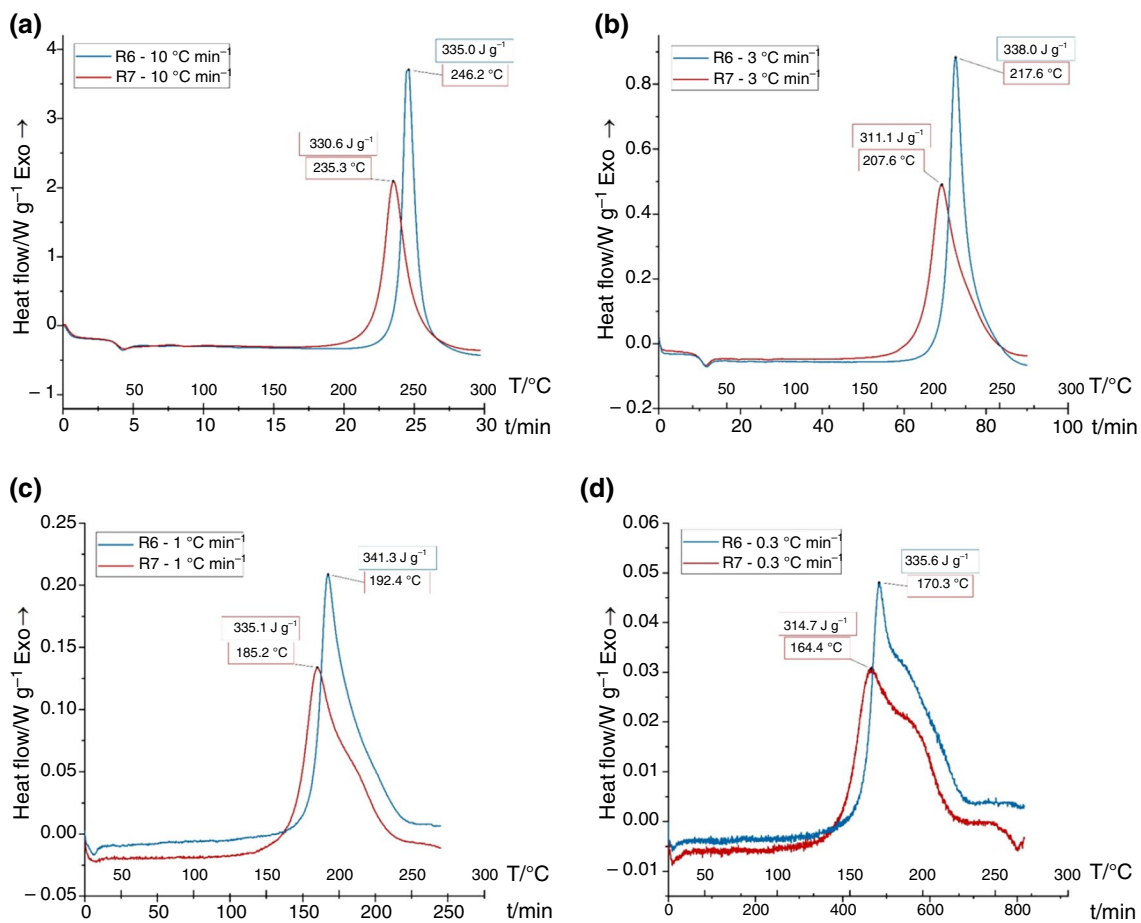


**Fig. 6** Comparison of R6 and R7 DSC curves obtained in N<sub>2</sub> atmosphere at (a) 10 °C min<sup>-1</sup>, (b) 3 °C min<sup>-1</sup>, (c) 1 °C min<sup>-1</sup> and (d) 0.3 °C min<sup>-1</sup> heating rate. The peak temperature and the energy of reaction of the main exothermic peak are indicated for each shown curve

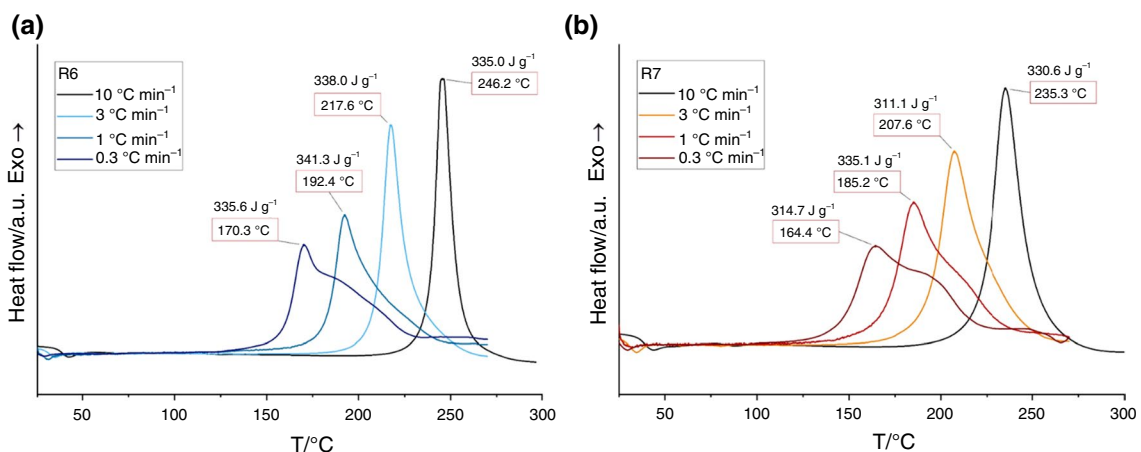


**Fig. 7** Area-normalized DSC curves obtained in N<sub>2</sub> atmosphere at different heating rates (10, 3, 1 and 0.3 °C min<sup>-1</sup>) for (a) R6 and (b) R7

case they show higher fluctuations but without any clear trend respect to the heating rate. Concerning the  $T_g$  values, those of R6 resin do not follow a monotone trend respect to the heating rate, and the highest values were registered

at 1 and 3 °C min<sup>-1</sup>, indicating the possible presence of a  $T_g$  maximum peak. In the R7 case, the glass transition temperature shows instead increasing values when decreasing the heating rate.

**Table 1** Exothermic peak temperature, crosslinking energy and glass transition temperature of R6 and R7 resins obtained through DSC analysis in N<sub>2</sub> atmosphere at different heating rates

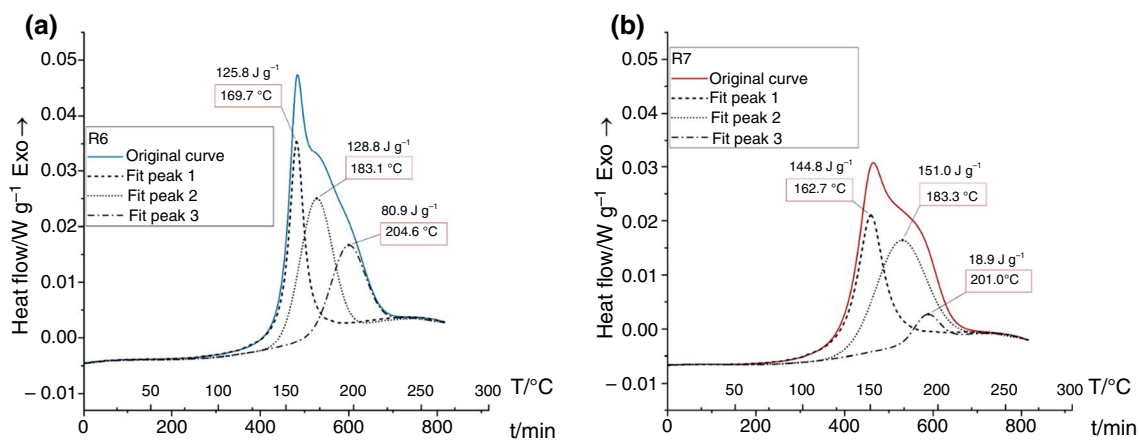
DSC heating rate	$T_{\text{peak}} / ^\circ\text{C}$		Crosslinking energy / $\text{J g}^{-1}$		$T_g$ (measured at $10^\circ\text{C min}^{-1}$ ) / $^\circ\text{C}$	
	R6	R7	R6	R7	R6	R7
$10^\circ\text{C min}^{-1}$	246.2	235.3	335.0	330.6	138.1	154.8
$3^\circ\text{C min}^{-1}$	217.6	207.6	338.0	311.1	158.4	156.8
$1^\circ\text{C min}^{-1}$	192.4	185.2	341.3	335.1	147.9	157.2
$0.3^\circ\text{C min}^{-1}$	170.3	164.4	335.6	314.7	143.2	194.5

While the DSC curve peaks obtained at 10 and  $3^\circ\text{C min}^{-1}$  have a symmetrical shape, those obtained at 1 and  $0.3^\circ\text{C min}^{-1}$  exhibit the presence of a shoulder on the right side of the  $T_{\text{peak}}$ , which appear more pronounced in the curves obtained at the lowest heating rate. These shoulders are separate peaks that result partially covered by the main peak, and can be explained by the presence of several reactions that contribute to the crosslinking process. The crosslinking of benzoxazine resins involves in fact potentially more than one reaction [24, 28], which depend on the different possible structural configurations of the starting monomers.

To further investigate the nature of the observed peak shoulders, a deconvolution of the  $0.3^\circ\text{C min}^{-1}$  curves was performed using OriginLab 2021 software. The results of this analysis are shown in Fig. 8. Both R6 (Fig. 8a) and R7 (Fig. 8b) deconvolutions indicate the presence of three different concurring reactions with comparable peak temperatures, which suggest that similar crosslinking reactions are involved in the curing of the two benzoxazine resins. However, R6 and R7 are distinguished by different magnitudes of these reactions, i.e. by different specific energy contributions. In fact, while the first two peaks show similar reaction energies for both resins, the third peak is much more pronounced in R6. Such difference in the third peak

contribution to the overall crosslinking reaction could explain the higher  $T_{\text{peak}}$  values observed for R6 respect to R7 at higher heating rates.

On the base of the calorimetric analyses carried out on the benzoxazine resins, compared to the conventional phenolic resin, it can be observed that the new resins show a crosslinking process composed of multiple steps, extending up to above  $200^\circ\text{C}$ , to have a complete curing. These observations are in agreement with literature data on similar resins [19, 28–30, 39–44]. Therefore, an industrial process for the production of brake pads including benzoxazine resin binder would be required to reach these temperatures during the curing stage. Examining the DSC curing curves, their deconvolution indicates the overlapping of three different peaks for both the new resins, R6 and R7, with R6 peaks falling at slightly higher temperatures (see Fig. 6). This can be attributed to the prominent contribution of the crosslinking reaction related to the third deconvoluted peak (see Fig. 8), which shows a much higher energy contribution respect to the equivalent one of the R7 resin. This result could be explained by the presence of methyl groups in R6 respect to the hydrogen atoms in R7 (see Fig. 1), since a higher steric hindrance of the chemical groups present in the resin monomer is known to hinder their polymerization rate [21].


**Fig. 8** Peak deconvolution of (a) R6 and (b) R7 at  $0.3^\circ\text{C min}^{-1}$  DSC curves, obtained in N<sub>2</sub> atmosphere. The peak temperature and the energy of reaction are indicated for each deconvoluted peak

### Kissinger analysis

The activation energy ( $E_a$ ) of the crosslinking reaction for both R6 and R7 was estimated using the Kissinger method. The original form of this method uses the  $T_{\text{peak}}$  recorded at different heating rates to evaluate the activation energy of the reaction associated to those peaks. However, this approach is prone to underestimating the kinetic complexity of reactions, especially when they involve a multistep process [28, 29], thus leading to meaningful errors in the evaluated  $E_a$ . By following an isoconversional approach, which involves the use of the temperatures corresponding to a fixed conversion rate of the reaction recorded at different heating rates, the error in the activation energy calculation can be minimized [45, 46]. Therefore, a Kissinger–Akahira–Sunose method [47] was hereby employed, following Eq. (3):

$$\ln\left(\frac{T_\alpha^2}{\varphi}\right) = \frac{E_{a(\alpha)}}{R \cdot T_\alpha} + \ln\left(\frac{E_{a(\alpha)}}{R \cdot k_0}\right) + \ln(\beta_\alpha) \quad (3)$$

where  $\alpha$  is the conversion rate of the transformation,  $T_\alpha$  is the temperature at which the  $\alpha$  value of conversion is reached,  $E_{a(\alpha)}$  is the activation energy required to reach  $\alpha$ ,  $\varphi$  is the heating rate,  $R$  is the universal gas constant,  $k$  is the pre-exponential factor, and  $\beta_\alpha$  is a constant (see “Appendix A1” section, Eq. (4)).

In the present investigation five different  $T_\alpha$  values were considered, i.e. those corresponding to  $\alpha$  values of 0.1, 0.3, 0.5, 0.7 and 0.9 for all the used heating rates, i.e. 10, 30, 50, 70 and 90% of the transformation energy. For each conversion percentage, the activation energy is then calculated by multiplying the universal gas constant  $R$  by the slope of the  $1/T_\alpha - \ln(T_\alpha^2/\varphi)$  plot. Table 2 shows the calculated  $T_\alpha$  and  $E_a$ , while Fig. 9 provides a comparison between the Kissinger plots obtained at different  $\alpha$  for both R6 (Fig. 9a) and R7

**Table 2** Temperature at which the conversion rate  $\alpha$  (0.1, 0.3, 0.5, 0.7 and 0.9) is reached at different heating rates and activation energy of the reactions involved to reach  $\alpha$  for R6 and R7

	$T_\alpha/^\circ\text{C}$				$E_a/\text{kJ mol}^{-1}$
	$0.3\text{ }^\circ\text{C min}^{-1}$	$1\text{ }^\circ\text{C min}^{-1}$	$3\text{ }^\circ\text{C min}^{-1}$	$10\text{ }^\circ\text{C min}^{-1}$	
R6 $_{\alpha=0.1}$	164.6	185.2	209.3	236.9	<b>81.5</b> ± 1.9
R7 $_{\alpha=0.1}$	152.5	173.2	194.6	221.6	<b>81.2</b> ± 1.1
R6 $_{\alpha=0.3}$	172.7	192.6	215.9	243.3	<b>86.5</b> ± 2.3
R7 $_{\alpha=0.3}$	164.3	184.1	204.7	231.6	<b>87.9</b> ± 2.0
R6 $_{\alpha=0.5}$	183.9	201.4	221.3	246.3	<b>102.3</b> ± 3.5
R7 $_{\alpha=0.5}$	175.5	194.9	212.1	236.7	<b>101.8</b> ± 2.6
R6 $_{\alpha=0.7}$	192.9	208.1	225.1	249.2	<b>117.4</b> ± 6.6
R7 $_{\alpha=0.7}$	186.7	203.5	218.8	241.7	<b>118.3</b> ± 4.6
R6 $_{\alpha=0.9}$	208.3	223.7	237.8	256.6	<b>146.3</b> ± 2.9
R7 $_{\alpha=0.9}$	201.9	221.0	232.9	252.8	<b>137.3</b> ± 7.9

In bold the activation energy is reported

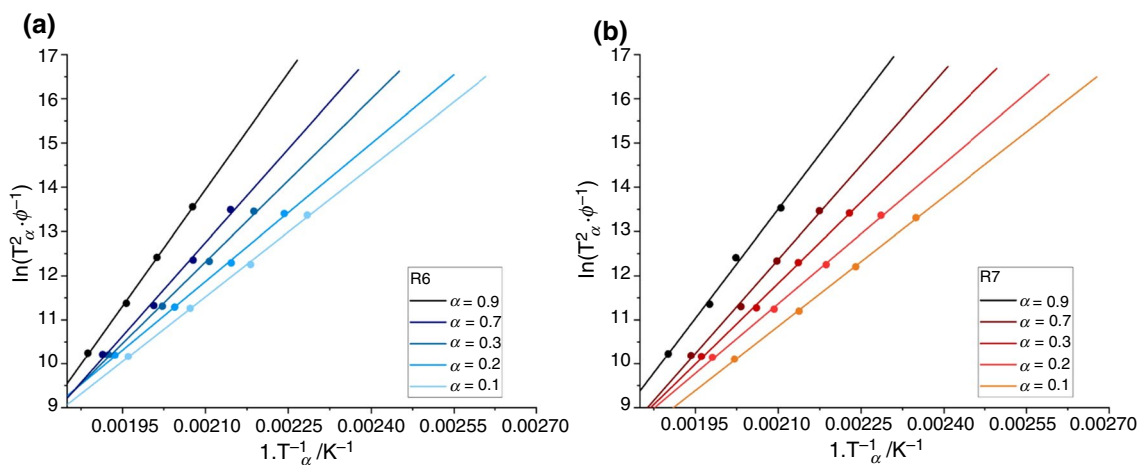


**Fig. 9** Kissinger plots of (a) R6 and (b) R7 at different progression percentages of the reaction. The slope of the fitted straight lines is indicative of the activation energy



(Fig. 9b). In all the investigated cases, the plotted values lead to good linear interpolation ( $R^2 > 0.993$ ). The activation energy of the transformation substantially increases (by 70–80%) with  $\alpha$ , further indicating that more than one step is involved in the crosslinking process of both R6 and R7 [48].

Curing process activation energy, measured through the Kissinger method, showed similar values between R6 and R7 for reaching the same degree of curing, suggesting that the involved curing mechanisms are mainly the same for the two resins. The steep increase in the activation energy required to reach higher curing degrees is in accordance with the results obtained from the deconvolution of the DSC peaks (see Fig. 8), further suggesting that the crosslinking process indeed involves more than a single step.

Further kinetic analysis was carried out by *Arrhenius method*, which produced results in line with the aforementioned ones. This analysis is reported in the “Appendix A3” section of the paper.

## Thermogravimetric analysis

### Inert atmosphere ( $N_2$ )

The full data regarding the degradation steps registered during TGA analysis in  $N_2$  atmosphere are reported in the “Appendix A4” section of the paper. Table 3 lists the mass loss value registered at 250 °C and 650 °C (respectively “ $m_{LOSS,250\text{ °C}}$ ” and “ $m_{LOSS,650\text{ °C}}$ ”) and the temperature corresponding to the maximum mass loss rate “ $T_{MLR}$ ” for all the samples that underwent thermogravimetric testing (i.e. resins in  $N_2$  and air and friction materials in air). The temperature of 250 °C was chosen as point of interest because it is representative of the operative conditions of disc brake systems, which under conventional braking conditions can reach about 200 °C [49, 50]. Figure 10 shows the TGA and DTG (Differential Thermogravimetric Analysis) curves obtained for R6, R7 and phenolic resin in nitrogen atmosphere. Both benzoxazine resins exhibit a lower mass loss in the initial part of the curve respect to Ph, but above ~300 °C their residual mass lowers below that of Ph. Indeed,  $m_{LOSS,250\text{ °C}}$  values of R6 and R7 are comparable,

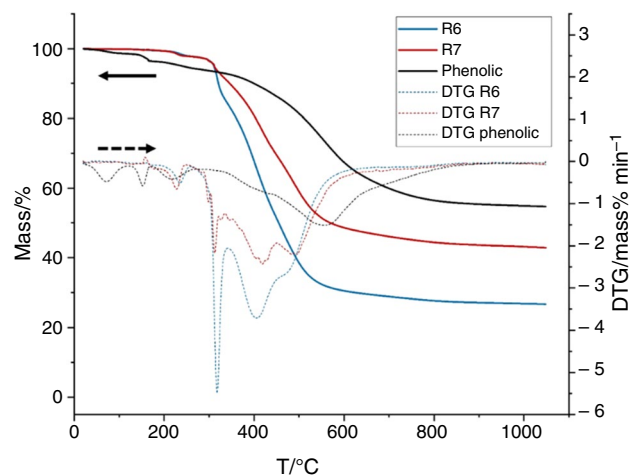


**Fig. 10** TGA and DTG curves of R6, R7 and Ph resins obtained in inert ( $N_2$ ) atmosphere

while being lower than half of that of Ph. The difference in  $T_{MLR}$  value between all the three resins suggests that, under nitrogen atmosphere, the reactions most affecting the mass loss of these materials are different. None of the three tested resins reach zero residual mass, in fact the lowest registered residual mass value (about 26%) at the end of the test was the one of R6.

Ran et al. [24] obtained comparable results to R6 with a similar benzoxazine resin based on BA-a. The higher mass residue of R7 respect to R6 might be due to different crosslinking structures formed during the curing of the resins, which will be later discussed. A difference in some curing mechanisms of the two resins was already suggested by the different contributions of the deconvoluted peaks shown in Fig. 8, and they might be ascribed to the steric hindrance of the dimethyl group present in the BA-a monomer (see Fig. 1).

### Air atmosphere

The full data regarding the degradation steps registered during TGA analysis in air atmosphere are reported in the

**Table 3** Mass loss percentages at 250 °C and 650 °C and temperature of max loss rate for R6, R7 and Ph in inert ( $N_2$ ) and air atmosphere

TGA	$m_{LOSS,250\text{ °C}}/%$			$m_{LOSS,650\text{ °C}}/%$			$T_{MLR}/\text{°C}$		
	R6	R7	Ph	R6	R7	Ph	R6	R7	Ph
Resins ( $N_2$ atmosphere)	2.04	2.17	5.31	70.45	52.82	37.08	318	418	555
Resins (Air atmosphere)	2.89	2.34	4.53	94.91	87.42	98.18	617	627	600
Friction mat (Air atmosphere)	0.81	0.57	0.75	12.74	13.71	16.99	744	753	531

The same parameters are also shown for the friction materials R6\_fm, R7\_fm and Ph\_fm in air atmosphere

“Appendix A4” section of the paper. Figure 11 shows the TGA and DTG curves obtained under air atmosphere for the three tested resins. Analogously to the results observed under nitrogen atmosphere, R6 and R7 exhibit lower mass loss respect to Ph at lower temperatures. Indeed, the  $m_{\text{LOSS},250^\circ\text{C}}$  values result at least 35% lower for the benzoxazine resins. Above approximately 300 °C, the phenolic resin maintains a higher residual mass, until about 600 °C. At the end of the test, all resins show a complete degradation, with mass losses above 98.5%, and only Ph reaching a value of 100%. In the reactive air atmosphere,  $T_{\text{MLR}}$  results similar for all three resins, suggesting that they have been subjected to the same degradation process.

A comparison between air-atmosphere TGA and DSC analyses of R6 and R7 is shown in Fig. 12. Both benzoxazine resins show an exothermic DSC peak in correspondence to

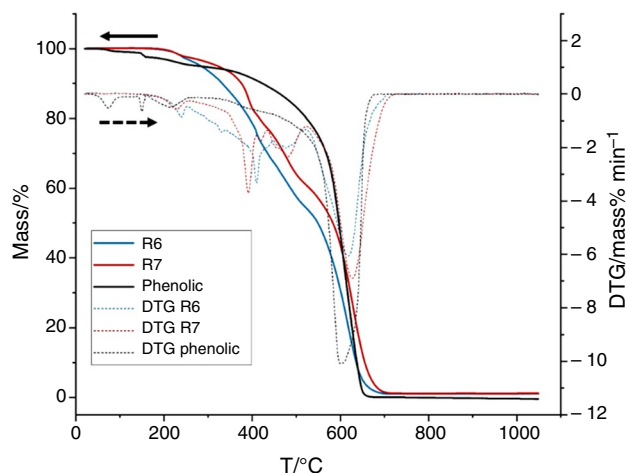


**Fig. 11** TGA and DTG curves of R6, R7 and Ph resins obtained in air atmosphere

the first DTG negative peak before 250 °C, thus indicating that the crosslinking process is responsible for the first mass loss stage.

As reported in other literature investigations, benzoxazine resins show a better temperature resistance than epoxy and phenolic resins [12, 13, 15, 19, 24]. In the present research, TGA analyses (see Fig. 11 and Table 3) demonstrated that the benzoxazine resins show an improved thermal behavior respect to the one of phenolic resin, at least concerning the range of application as binder for brake pads, i.e. 200–250 °C in case of severe braking actions. Lower  $m_{\text{LOSS},250^\circ\text{C}}$  values were in fact registered both in inert  $\text{N}_2$  atmosphere and in a more operation-representative air atmosphere (see Figs. 10, 11 and Table 3).

While R6 and R7 resins have extremely similar monomer molecules, the thermal analyses showed some differences in their properties. The four main crosslinking structures that have been proposed for the curing of polybenzoxazines resins [24, 51–53] are shown in Fig. 13, in clockwise decreasing order of stability. Since R7 displayed slightly better thermal degradation properties, in both  $\text{N}_2$  and air atmosphere, respect to those of R6, it is supposed that R7 was able to either produce a higher fraction of *arylamine Mannich bridge* (Fig. 13c) structures or a lower fraction *Mannich base phenoxy-type bridge* (Fig. 13e) structures respect to R6. Since the overall crosslinking energy of R7 always resulted lower than that of R6 (see Table 1), it is unlikely that the higher thermal stability of R7 could be explained by a higher crosslinking degree. Thus, the capability to form more stable linkages appears to be a more reasonable explanation.

The reaction associated to the third deconvoluted peak, shown in Fig. 8, might be therefore the one resulting in one of the less stable linking structures, since it is more prevalent in the case of R6. The reason for the formation of different crosslinking structures between R6 and R7 might

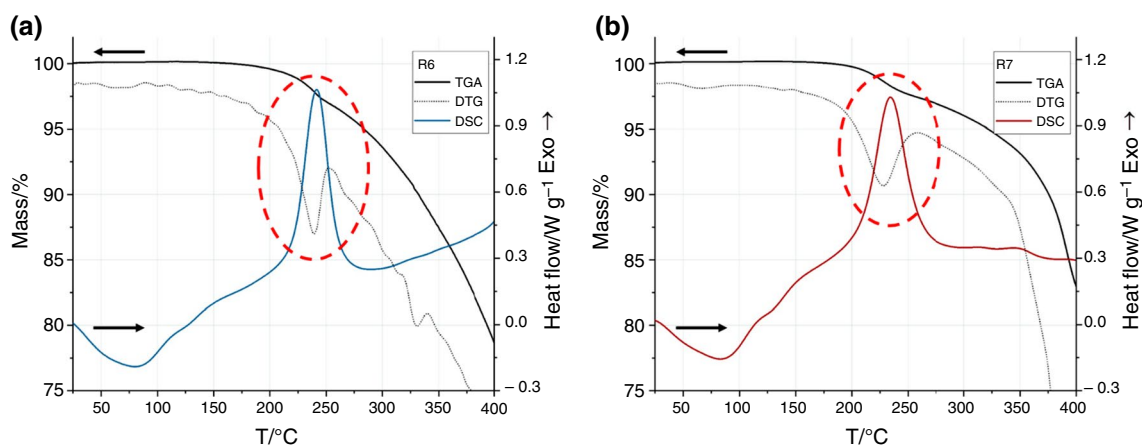
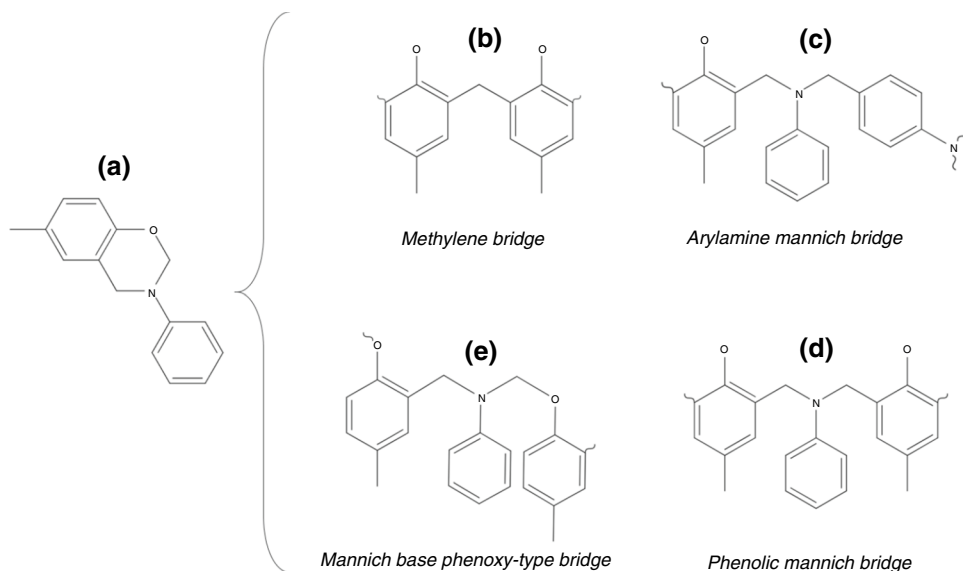


**Fig. 12** TGA, DTG (scale not reported) and DSC curves of (a) R6 and (b) R7 obtained in air atmosphere. The red dashed circle indicates the exothermic peak of the DSC curve and the correspondent negative DTG curve peak

**Fig. 13** Possible crosslinking structures that can be formed during the curing process of a benzoxazine resin. (a) is a general benzoxazine monomer. The crosslinking structures are, in decreasing order of thermal stability: methylene bridge (b), arylamine Mannich bridge (c), phenolic Mannich bridge (d) and Mannich base phenoxy-type bridge (e)



be identified in the previously discussed effect of the steric hindrance of the R6 dimethyl group, which can influence the crosslinking process [21].

### Friction materials in air atmosphere

Figure 14 reports the TGA and DTG curves of the R6\_fm, R7\_fm and Ph\_fm friction materials in air atmosphere. Figure 14b shows a magnification of the results obtained in the 0–400 °C range. At 250 °C, R7\_fm undergoes a lower mass loss than that of R6\_fm and Ph\_fm, which instead share a similar value of  $m_{\text{LOSS},250\text{ }^\circ\text{C}}$ . Above 300 °C the TGA curves of all three resins behave similarly, up until 490 °C, where the mass loss rate of the benzoxazine-containing friction materials start to stabilize while that of Ph\_fm continues

to increase (see circled portion of DTG curves in Fig. 14a). This leads to values of  $m_{\text{LOSS},650\text{ }^\circ\text{C}}$  that are more than 20% lower for the R6\_fm and R7\_fm friction materials respect to the Ph\_fm one. These  $m_{\text{LOSS},650\text{ }^\circ\text{C}}$  results diverge from those obtained from the analyses of the resins, where Ph showed a lower mass loss respect to the benzoxazine resins, suggesting that the curing process has better stabilizing effect on R6 and R7. It is also worth noting that the  $m_{\text{LOSS},250\text{ }^\circ\text{C}}$  values of the three friction materials exceed the 7% value, indicating that other constituents of the friction materials over the resins (e.g. rubber, aramid fibre, vermiculite and mica [54, 55]) are also degrading.

Whilst the neat resins TGA curves reached a plateau shortly after 650 °C, those of the friction materials show a further mass loss of around 10% followed by an increase

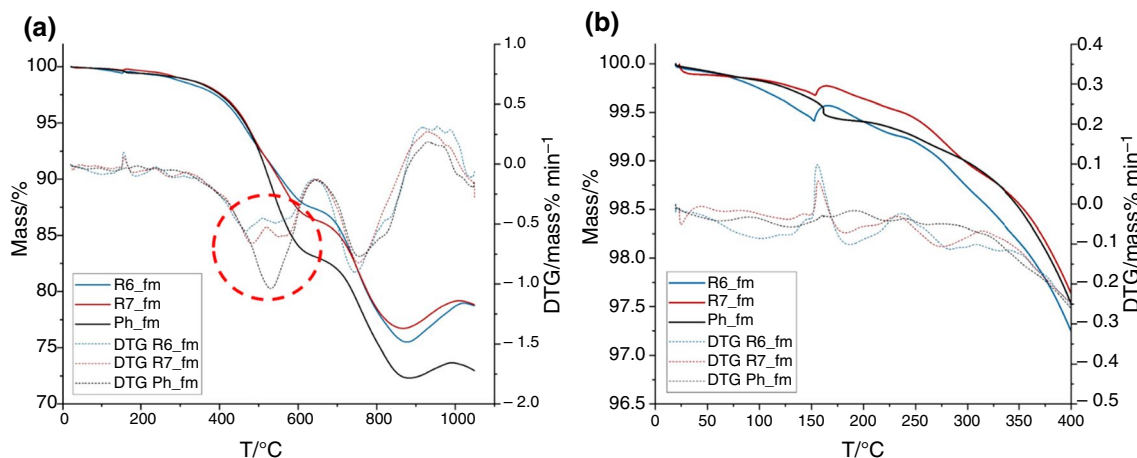


**Fig. 14** TGA and DTG curves of R6\_fm, R7\_fm and Ph\_fm friction materials obtained in air atmosphere. The full range of analysis is shown in (a), while (b) shows the curves up until 400 °C. The red

dashed circle in (a) highlights the point where the Ph\_fm DTG curve noticeably departs from those of R6\_fm and R7\_fm (~490 °C)

of the registered mass. The mass loss can be explained by the degradation of other ingredients present in the friction material mixture, e.g. vermiculite, graphite and coke [54, 56, 57], which also contribute to the maximum mass loss rate in the case of R6\_fm and R7\_fm. The mass increase observed above 800 °C is related to the oxidation of metallic constituents present in the friction material like Fe fibres.

The thermal behavior of the friction materials produced using R6 and R7 resins, i.e. the pad materials, resulted similar to that produced with phenolic resin, in the temperature range up to 250 °C, as shown in Fig. 14b. Starting from this temperature an incipient phenomenon of brake pad fading, due to overheating, may occur [58, 59]. The similar TGA curves up to 250 °C indicates the feasibility of substituting the phenolic resin with the new ones, without any risk of having a higher or earlier pad degradation process. In this regard, it is worth noting that R6\_fm and R7\_fm showed satisfactory thermal degradation resistance even though the production process involved a hot moulding stage which was not optimized for their higher temperature curing. In order to promote the development of the crosslinking reaction already during the hot moulding stage, a temperature in excess of 150 °C is required. It is also important to note that the hot moulding parameters required to optimize the friction material production would change depending on the particular type of benzoxazine resin employed, which would have their crosslinking further influenced by the applied pressure, as shown by Zeng et al. [22].

### Shore D hardness

The results of the Shore D hardness tests, which were performed applying a 4 kg load, are listed in Table 4. The values obtained for the cured R6 and R7 resins are comparable, and similar to a control epoxy resin that showed an average shore D hardness of 86. In the case of friction materials, R6\_fm and R7\_fm show similar results, with R7\_fm being slightly harder. However, Ph\_fm shows a clearly higher hardness value respect to those of the other two friction materials. This discrepancy can be explained by the difference in the densities of the friction materials. In fact, a higher density leads to higher shore D values, as depicted in Fig. 15. The comparable values of R6\_fm and R7\_fm are expected due

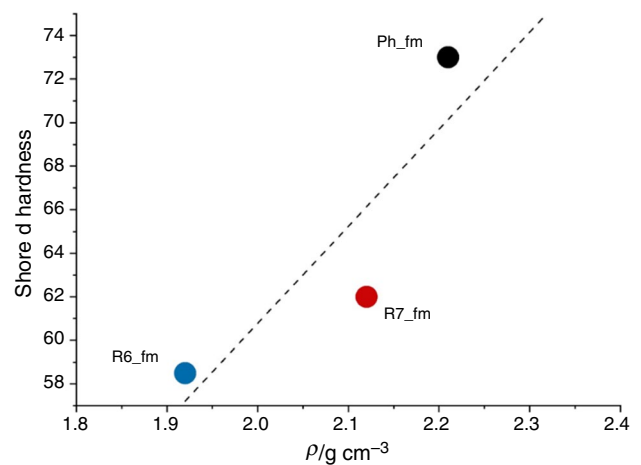


**Fig. 15** Shore D hardness variation with density of friction materials R6\_fm, R7\_fm and Ph\_fm. The dashed line shows the linear fitting of the plotted points

to the high similarity in composition between the compared materials, which only slightly differ in their binder.

For all materials, the measurements taken on the pin friction surface (reported in Table 4) showed an increase in the shore D hardness value of 3.5–4, which is attributable to the formation of a so-called “friction layer” [60, 61] on the mating surfaces during the Pin on Disc testing. In fact, the friction layer is constituted by compacted wear fragments, in particular by oxidized metallic particles [1, 5].

Hardness values of the friction materials produced with the new resins are in the range of the reference one, even if a slightly lower density has been measured in R6\_fm and R7\_fm. The density difference itself does not arise from a disparity between the densities of the resins, but it might be a by-product of the adopted hot moulding production step. While the curing step was adapted to the friction material binder resin, i.e. it was the same used for the neat resins (see Fig. 3), it is crucial to note that, in the production route of the friction materials, a hot moulding operation was performed before the curing stage.

As shown in Table 5, the benzoxazine-containing friction materials are subjected to stronger mass loss and larger height expansion during the curing process respect to those observed for Ph\_fm, which lead to a higher density loss. In

**Table 4** Shore D hardness and bulk density of R6 and R7 resins and of R6\_fm, R7\_fm and Ph\_fm friction materials

	R6	R7	R6_fm	R6_fm contact surface	R7_fm	R7_fm contact surface	Ph_fm	Ph_fm contact surface
Shore D (4 kg load)	87.9 ± 2.5	84.5 ± 4.7	58.5 ± 2.7	62.8 ± 2.9	62.0 ± 2.0	65.5 ± 3.8	73.0 ± 2.0	76.7 ± 1.5
Bulk density /g cm <sup>-3</sup>	1.21	1.26	1.92	-	2.12	-	2.21	-

The shore D hardness value is also shown for the surfaces of R6\_fm, R7\_fm and Ph\_fm that underwent tribological testing

**Table 5** Density difference, height expansion and mass loss caused by the curing process of R6\_fm, R7\_fm and Ph\_fm friction materials

Friction material	Curing $\Delta\rho$ /g cm <sup>-3</sup>	Curing height growth /%	Curing mass loss /%	Neat resins curing mass loss /%
R6_fm	-0.53	22	0.9	1.0
R7_fm	-0.49	19	0.7	0.5
Ph_fm	-0.34	13	0.6	4.5

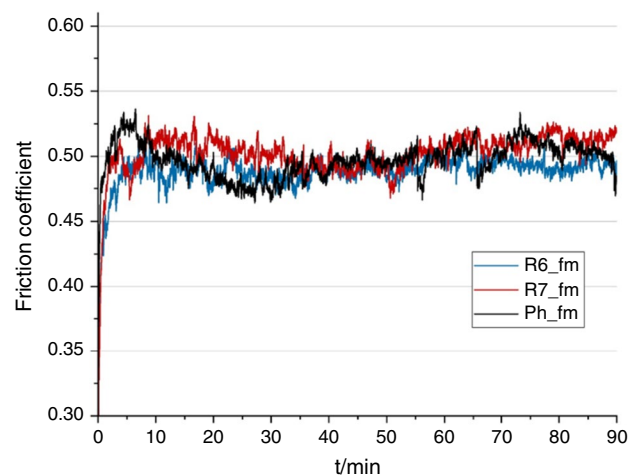
The mass loss during curing is also shown for the neat R6, R7 and Ph resins subjected to the same curing process

spite of this, the curing mass loss of the neat resins exhibits the opposite behavior, i.e. Ph loses more mass respect to both R6 and R7. This discrepancy between neat resin and friction material mass losses can be attributed to the hot moulding process, which was performed at the machine limit value of 150 °C. For R6 and R7, this temperature falls below the  $T_{peak}$  of their crosslinking reaction, while it is well above that of Ph (see Fig. 5). Therefore, the hot moulding step allowed for a significant evolution of the binder crosslinking, before undergoing the specific curing stage process, only in the case of Ph\_fm. This entails that, for Ph\_fm, a portion of the density loss associated to the resin crosslinking reaction was compensated by the hot moulding pressure application. Nevertheless, a lower density, or higher porosity, in a friction material is not necessarily detrimental, as it can have some beneficial effects with respect to braking noise [10, 62].

### Pin-on-disc tribological testing

Single samples of R6\_fm, R7\_fm and Ph\_fm were tested on a pin-on-disc tribometer in order to assess the feasibility of the application of benzoxazine resins as friction material binders. While single test run values do not provide a conclusive picture of the tribological performances of the new materials, they are enough to evaluate if their overall behavior complies with their intended application. Figure 16 shows the friction coefficient evolution of the three friction materials during the pin-on-disc test.

The three pin-on-disc curves show a similar behavior. Two specific parts of the COF curves can be distinguished in each curve, namely a “run-in” period and a “steady-state” regime. The run-in is the brief time window at the beginning of each test during which the friction coefficient rapidly increases. The steady-state regime is achieved once the friction coefficient curve stabilizes. R6\_fm and R7\_fm reach this steady-state faster respect to Ph\_fm and show an overall more stable behavior of the friction coefficient. Once the steady-state is reached, the friction coefficient results are almost identical, as shown in Table 6.


**Fig. 16** Pin-on-disc friction coefficient curves of R6\_fm, R7\_fm and Ph\_fm friction materials

The calculated values of steady-state friction coefficient, specific wear coefficient (“Ka”) of the pin and of the disc, and the “pin specific wear” are listed in Table 6.

The benzoxazine-containing friction material pins show similar Ka values, while that of Ph\_fm is lower. However, Ka is a measure of the volumetric wear, and it is therefore influenced by the density difference between the tested materials. Therefore, while Ka is still a valuable measure of the wear of these friction materials, the mass loss is more representative of the amount of material worn during the test and is represented by the *pin specific wear* of the tested samples, which was measured as the mass loss over the total slid distance. In this case, R6\_fm and Ph\_fm show the same mass wear, while R7\_fm loses more mass per unit of travelled distance.

The specific wear coefficients of the cast iron discs reflect the ones obtained for the pin specific wear, i.e. R6\_fm and Ph\_fm show similar results, while R7\_fm displays higher wear. Note that there would be no relative difference between the volume and mass wear of the discs because the disc material is always the same.

The tribological properties of the friction materials produced with R6 and R7 resins are the most important

**Table 6** Steady-state friction coefficient ( $\mu$ ), specific wear coefficient of the pin ( $K_a$ ) and of the disc ( $K_{a_{DISC}}$ ), and pin specific wear of R6\_fm, R7\_fm and Ph\_fm friction materials obtained through Pin-on-Disc testing

	R6_fm	R7_fm	Ph_fm
$\mu$ (steady-state)	0.49	0.50	0.50
$K_a/10^{-14} \text{ m}^2 \text{ N}^{-1}$	3.53	3.57	3.01
$K_{a_{DISC}}/10^{-14} \text{ m}^2 \text{ N}^{-1}$	1.49	1.71	1.47
Pin specific wear/mg km <sup>-1</sup>	5.3	6.0	5.3

characteristics when considering the application of benzoxazines as binder for brake pads. Notably, the friction coefficients, measured during pin-on-disc tests sliding against a cast iron disc, showed the same values observed in the case of the pin made with phenolic resin (0.49–0.50). COF is indicative of the braking efficiency of the pad + disc system, and it must in fact be in a precise range for the automotive applications to ensure a stable and reliable braking action. Therefore, the preservation of the  $\mu$  level is an optimal result from a brake pad application standpoint.

Regarding the pin wear, in terms of mass loss, it also resulted very similar for the three friction materials, whereas in terms of volume loss, wear appeared slightly higher for benzoxazine-containing friction materials, since these have lower density than the phenolic based one. It is important to stress that these preliminary tribological tests were carried out in mild braking conditions, which led to disc temperatures not exceeding 50 °C. As it was presented in the thermal analysis sections of this work, the benzoxazine resins (and friction materials containing them) should present some advantages respect to the conventional phenolic resin when subjected to harsher conditions, i.e. in the case of heavier braking conditions (higher temperature).

In perspective, the optimization of the processing temperatures/times, in particular those of the hot moulding stage, would lead to the production of benzoxazine based friction materials with superior properties, able to ensure higher temperature resistance if tested in conditions of more severe braking. This also entails that a lower environmental/health impact would be expected by the lowering of produced emission related to both the pad wear ( $PM_{10}$ ) and resin degradation ( $PM_1$ ). Dynamometric tests simulating real braking conditions will be also carried out to assess the performance of the new friction materials.

Overall, the tribological test results indicate that benzoxazine resins can successfully be implemented as binder for friction materials.

## Conclusions

Two different benzoxazine resins were studied and compared with a conventional phenolic resin in order to assess the possibility to use them as binder in automotive brake pads. Both neat resins and friction materials containing them were tested, providing some interesting results:

- The curing reaction of the R6 and R7 benzoxazine resins is a multistep process, as indicated by DSC and Kissinger analyses
- Despite the longer time requirements, a slow heating rate seems preferable to investigate benzoxazine resins, in order to better assess the multistep reaction

- An activation energy above 140 kJ mol<sup>-1</sup> is required to reach complete crosslinking of R6 and R7
- R7 showed slightly better resistance to thermal degradation respect to R6. An easier capability to form more stable crosslinking structures during curing was indicated as main possible explanation
- The benzoxazine resins show better thermal resistance respect to the phenolic resin, especially in the temperature range of interest (< 250 °C)
- Friction materials with benzoxazine resin binder offer satisfactory tribological properties, suggesting promising capabilities if produced following a better optimized process
- The thermal properties shown by the benzoxazine resins suggest that the friction materials containing them are poised to provide better braking capabilities than those of friction materials containing phenolic resin in the case of more severe braking conditions, while also lowering their particulate matter production

## Appendix

### A1: State function for Kissinger analysis

For constant heating rates, the state function  $\beta$  follows Eq. (4) [63]:

$$\beta = \frac{T^2}{\varphi} \cdot \frac{R}{E_a} \cdot k_0 \quad (4)$$

For a fixed conversion percentages of the reaction ( $\alpha$ ), the value of  $\beta_\alpha$  remains constant when varying the heating rate  $\varphi$  [63].

### A2: Curing steps effects

The DSC curves for the 145 °C/3 h, 145 + 170 and 145 + 190 samples, obtained with a 10 °C min<sup>-1</sup> heating rate, are shown in Fig. 17. Similarly to the results obtained for the neat resins (see Fig. 6), the R6 curves show peak temperatures higher than those of R7. The reaction energies obtained from the area of these curves represent the residual portion of the crosslinking reaction, which was not brought to completion by the performed heat treatments. In Fig. 18, the effect of the heat treatments on the DSC curves of the tested resins can be better appreciated. Indeed, Fig. 18 clearly shows how the crosslinking peaks shift to higher temperatures and give lower residual energies when moving from the 145 °C/3 h treatment to the 145 + 170 and further to the 145 + 190 treatments.

Table 7 lists the peak temperature, the crosslinking energy and both the  $T_g$  and the post-DSC  $T_g$  (referred to as

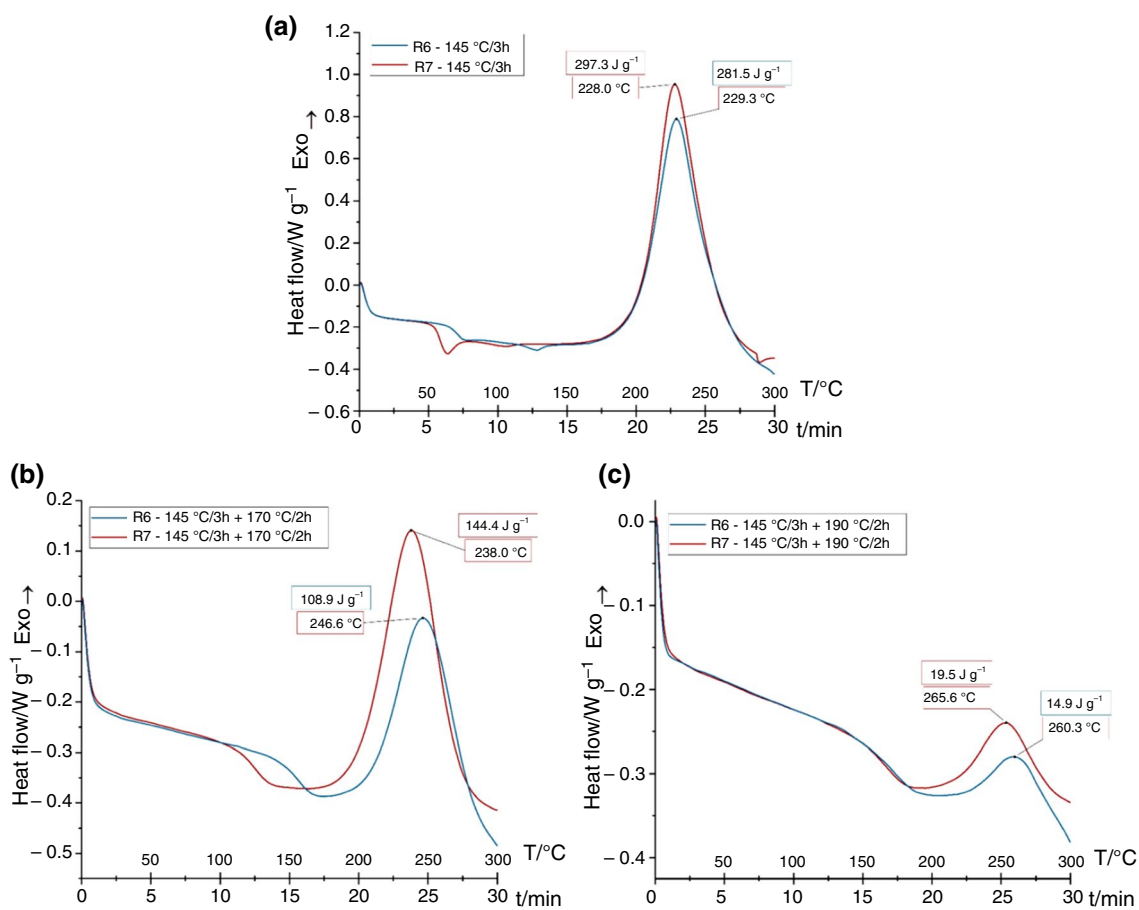


**Fig. 17** 10 °C min<sup>-1</sup> DSC curves of R6 and R7 samples that underwent the (a) 145 °C/3 h, (b) 145 + 170 and (c) 145 + 190 treatments under N<sub>2</sub> atmosphere

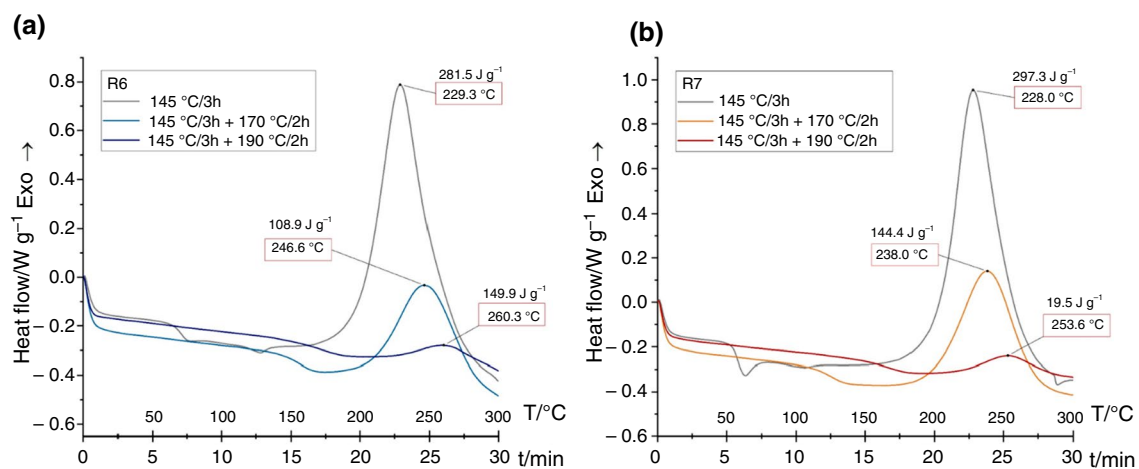


**Fig. 18** 10 °C min<sup>-1</sup> DSC curves of the 145 °C/3 h, 145 + 170 and 145 + 190 treatments of (a) R6 and (b) R7 under N<sub>2</sub> atmosphere

$T_{gI}$  and  $T_{gII}$ , respectively) of the analysed samples. Note that  $T_{gI}$  is the value that showcases the effects of the 145/3 h, 145 + 170 and 145 + 190 thermal treatments, while  $T_{gII}$

is influenced by the thermal treatment related to the DSC analysis heating. By comparing these results with the ones obtained for the neat resins (see Table 1), the 145 °C/3 h

**Table 7** Peak temperature, energy of the exothermic peak and glass transition temperature of first and second 10 °C min<sup>-1</sup> DSC scan performed on R6 and R7 samples that underwent the 145 °C/3 h, 145 + 170 and 145 + 190 thermal treatments

Curing steps (DSC performed at 10 °C min <sup>-1</sup> )	T <sub>peak</sub> /°C		Residual energy /J g <sup>-1</sup>		T <sub>gI</sub> (first scan) /°C		T <sub>gII</sub> (second scan) /°C	
	R6	R7	R6	R7	R6	R7	R6	R7
145 °C/3 h	229.3	228	281.5	297.3	69.5	57.1	135.7	134.1
145 °C/3 h + 170/2 h	246.6	238	108.9	144.4	155.6	124.5	153.6	171.7
145 °C/3 h + 190/2 h	260.3	253.6	14.9	19.5	171.8	167	160.5	178.4

**Table 8** Heating rate and peak temperature data of the DSC analyses in N<sub>2</sub> atmosphere performed on R6 and R7

φ /°C min <sup>-1</sup>	Log(φ)	R6 T <sub>peak</sub> /°C	R7 T <sub>peak</sub> /°C	R6 T <sub>peak</sub> /K	R7 T <sub>peak</sub> /K	R6 T <sub>peak</sub> <sup>-1</sup> /K <sup>-1</sup>	R7 T <sub>peak</sub> <sup>-1</sup> /K <sup>-1</sup>
10	1	246,2	235,3	519,36	508,46	0,001,925	0,001,967
3	0,477,121	217,6	207,6	490,76	480,76	0,002,038	0,002,08
1	0	192,4	185,2	465,56	458,36	0,002,148	0,002,182
0,3	- 0,52,288	170,3	164,4	443,46	437,56	0,002,255	0,002,285

treatment shows marginal effects towards the development of the crosslinking process. It still exhibits 84–90% of residual crosslinking energy, comparable values of T<sub>peak</sub>, and much lower values of T<sub>gI</sub>. The 145 + 170 treatment displays a progression in the crosslinking process instead: residual energy is in the 32–44% range and T<sub>peak</sub> increases, suggesting that the crosslinking phenomena that develop at lower temperatures have been carried out, at least partially, thus leaving the higher temperature ones to be detected by the DSC analysis as curve residues (see Fig. 8). T<sub>gI</sub> is higher than the one recorded for the post-DSC neat R6 resin, while that of R7 is still lower. The 145 + 190 treatment results indicate almost complete crosslinking: residual energy is 4–6%, T<sub>peak</sub> is further increased, and T<sub>gI</sub> values are higher than all those previously recorded, suggesting that a multistep curing process allows for a better development of the crosslinking network of these resins.

### A3: Analysis of the multistep reaction

In the dynamic method derived from the Arrhenius method, several heating rates are used and they are related to the temperature at which definite percentage of crosslinking occurs, according to Eq. (5):

$$\log(\varphi) = A - \frac{E_a}{2.303 \cdot R \cdot T_\alpha} \quad (5)$$

where φ is the heating rate, A is the pre-exponential factor, E<sub>a</sub> is the activation energy, R is the universal gas constant, and T<sub>α</sub> is the absolute temperature at which an α percentage of crosslinking has been completed.

The peak temperatures of R6 and R7 registered during DSC analysis in N<sub>2</sub> atmosphere at different heating rates,

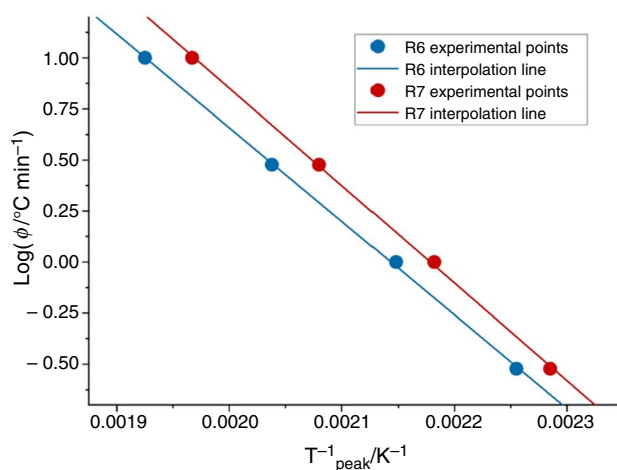


**Fig. 19** Line interpolation of the heating rate and T<sub>peak</sub> data obtained from the DSC analysis of R6 (blue line) and R7 (red line)

and the heating rate values of each analysis are reported in Table 8.

Figure 19 shows the Arrhenius interpolated straight lines of R6 and R7 obtained from plotting T<sub>peak</sub><sup>-1</sup> and log(φ) obtained by DSC analysis. From these lines, it was possible to calculate the activation energy E<sub>a</sub> and the pre-exponential factor A for the crosslinking reactions of R6 and R7, which are, respectively, related to the slope and the intercept of the lines. E<sub>a</sub>, A and the interpolated straight lines data are reported in Table 9. The pre-exponential factor A represents the log(φ) at which a certain percentage of crosslinking occurs at infinite temperature; the higher the value, the faster the reaction. Note that the peak positions seem to correspond to the value of about 30% of the crosslinking reaction (see Table 2). The kinetics of the thermal crosslinking



**Table 9** Straight line data, pre-exponential factor (A) and activation energy ( $E_a$ ) obtained from the interpolation of the heating rate and  $T_{peak}$  of R6 and R7 DSC analyses

	$^{\circ}\text{C min}^{-1 2}$	slope	A (intercept)	$E_a$ /kJ mol $^{-1}$
R6 peak	0,99,928	$-4586 \pm 71$	$9,83 \pm 0,15$	$87.8 \pm 1.4$
R7 peak	0,99,926	$-4776 \pm 75$	$10,41 \pm 0,16$	$91.4 \pm 1.4$

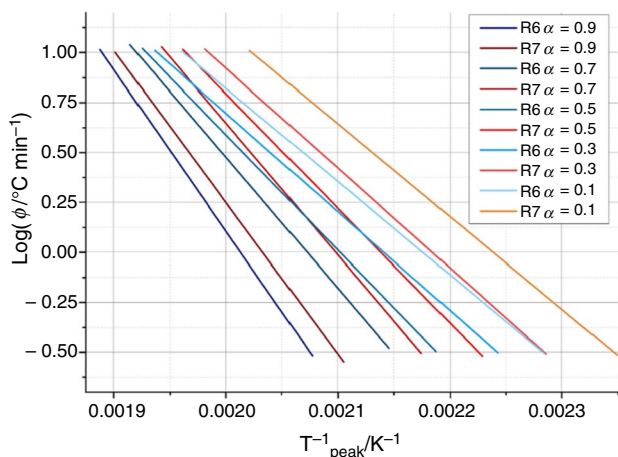
process depend on both the activation energy and on the pre-exponential factor. The higher A value of R7 indicates that its crosslinking reaction occurs faster respect to that of R6.

The interpolated straight lines obtained from the Arrhenius analysis of the DSC curves at different  $\alpha$  values (0.1, 0.3, 0.5, 0.7 and 0.9) are shown in Fig. 20. The data relative to the interpolated lines, as well as the activation energies  $E_a$  are reported in Table 10.

The activation energies obtained following the Arrhenius approach result coherent with those calculated following the Kissinger–Akahira–Sunose method. However, their value is consistently higher by about 9 kJ mol $^{-1}$ .

Figure 21 shows the behavior of the activation energy  $E_a$  and pre-exponential factor A respect to the evolution of the crosslinking reaction  $\alpha$  of R6 and R7.  $E_a$  and A show analogous trends for both R6 and R7. Both  $E_a$  and A result higher for R6 to reach 90% of the crosslinking reaction respect to R7. These results match those obtained with the Kissinger–Akahira–Sunose method (see Table 2), and they are also in agreement with the peak deconvolution shown in Fig. 8. The higher value of  $E_a$  and A in case of R6 $_{\alpha=0.9}$  is in fact representative of the third deconvoluted peak, which is larger than its R7 counterpart.

Furthermore, for both resin, in Fig. 21 it is possible to appreciate three different curve trends that can be attributed to the three reaction peaks shown in Fig. 8. The first is below


**Fig. 20** Line interpolation of the heating rate and  $T_{\alpha}$  data obtained from the DSC analysis of R6 (blue lines) and R7 (red lines)

**Table 10** Straight line data, pre-exponential factor (A) and activation energy ( $E_a$ ) obtained from the interpolation of the heating rate and  $T_{peak}$  of R6 and R7 DSC analyses

Resin	$R^2$	slope	A (intercept)	$E_a$ /kJ mol $^{-1}$
R6 $_{\alpha=0.1}$	0,99,876	$-4668 \pm 95$	$10,16 \pm 0,20$	$89.4 \pm 1.8$
R7 $_{\alpha=0.1}$	0,99,962	$-4641 \pm 52$	$10,39 \pm 0,11$	$88.9 \pm 1.0$
R6 $_{\alpha=0.3}$	0,99,834	$-4933 \pm 116$	$10,56 \pm 0,24$	$94.5 \pm 2.2$
R7 $_{\alpha=0.3}$	0,99,882	$-4998 \pm 99$	$10,92 \pm 0,21$	$95.7 \pm 1.9$
R6 $_{\alpha=0.5}$	0,99,717	$-5768 \pm 177$	$12,12 \pm 0,37$	$110.4 \pm 3.4$
R7 $_{\alpha=0.5}$	0,99,836	$-5735 \pm 134$	$12,26 \pm 0,28$	$109.8 \pm 2.6$
R6 $_{\alpha=0.7}$	0,99,208	$-6563 \pm 338$	$13,60 \pm 0,69$	$125.7 \pm 6.5$
R7 $_{\alpha=0.7}$	0,9962	$-6600 \pm 234$	$13,85 \pm 0,48$	$126.4 \pm 4.5$
R6 $_{\alpha=0.9}$	0,9990	$-8083 \pm 148$	$16,27 \pm 0,29$	$154.8 \pm 2.9$
R7 $_{\alpha=0.9}$	0,99,103	$-7603 \pm 417$	$15,46 \pm 0,84$	$145.6 \pm 8.0$

$\alpha = 0.3$ , the second between  $\alpha = 0.3$  and  $\alpha = 0.7$ , and the third one above  $\alpha = 0.7$ . In the case of R7, the curve trend above  $\alpha = 0.7$  shows little difference respect to the previous part of the curve, and this is explained by the low energy contribution of the third reaction during its crosslinking (see Fig. 8b).

#### A4: Thermogravimetric analysis data

The thermal degradation events of Ph, R6 and R7 that developed during TGA analysis in  $N_2$  atmosphere (see Fig. 10) were identified as the negative peaks on the relative DTG curve. The temperatures of start ( $T_s$ ) and finish ( $T_f$ ) of these steps, as well as their mass loss (both of the single event and the total mass loss reached) are reported in Tables 11, 12 and 13.

While certain degradation steps were easily distinguishable and their contribution to the mass loss clearly identifiable, other events were influenced by multiple concurring reactions. Their DTG peaks, while discernible, behaved like shoulders on a broader background peak. Therefore, their  $T_s$ ,  $T_f$  and mass loss values are not unequivocally representative of their own contribution. In particular, Ph event 3, R6 events 2 and 3 and R7 events 2, 3, 4 and 5 show some overlap of diverse events in  $N_2$  atmosphere. As an example, the shoulder on the DTG peak of R6 event 3 suggests that it comprises the contributions of R7 events 4 and 5. Furthermore, it should be noted that all the TGA curves reached their maximum mass loss at the end of the test, i.e., at 1050  $^{\circ}\text{C}$ , suggesting that some more degradation, although minimal, could have been still developing.

The thermal degradation events of Ph, R6 and R7 that developed during TGA analysis in air atmosphere (see Fig. 11) were identified as the negative peaks on the relative DTG curve. The temperatures of start ( $T_s$ ) and finish ( $T_f$ ) of these steps, as well as their mass loss (both of the

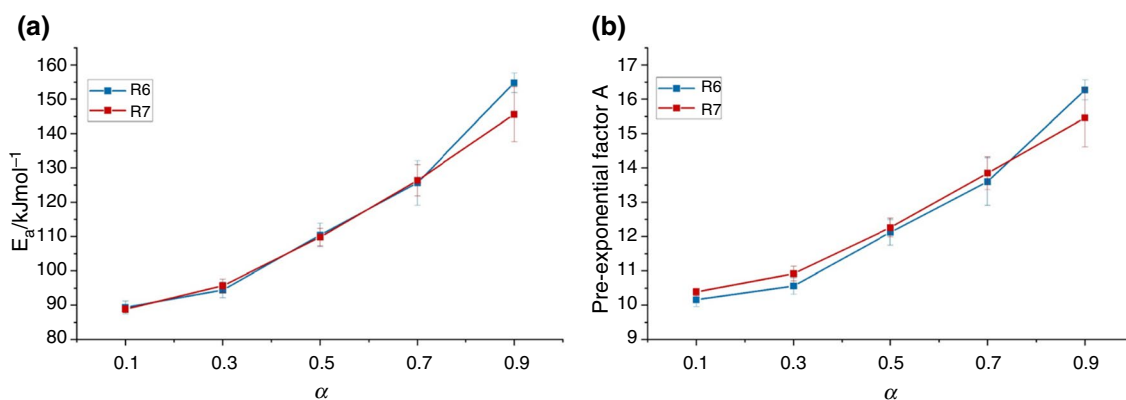


**Fig. 21** Dependency of activation energy  $E_a$  (a) and pre-exponential factor A (b) on development of the crosslinking reaction ( $\alpha$ ) in case of R6 and R7

**Table 11** Degradation step start ( $T_s$ ) and finish ( $T_f$ ) temperatures, mass loss contribution of the single degradation step and total mass loss reached after the step registered by TGA analysis of Ph resin in  $N_2$  atmosphere

Ph $N_2$ event #	$T_s$ /°C	$T_f$ /°C	Event mass loss /%	Total mass loss /%
1	28.6	120.3	1.5	1.5
2	125.7	171.9	2.1	3.6
3	175.0	276.2	2.3	5.9
4	297.1	1050	39.2	45.3

**Table 12** Degradation step start ( $T_s$ ) and finish ( $T_f$ ) temperatures, mass loss contribution of the single degradation step and total mass loss reached after the step registered by TGA analysis of R6 resin in  $N_2$  atmosphere

R6 $N_2$ event #	$T_s$ /°C	$T_f$ /°C	Event mass loss /%	Total mass loss /%
1	166.5	260.2	2.2	2.2
2	263.4	340.2	13.5	15.7
3	344.3	1050	67.7	73.4

**Table 13** Degradation step start ( $T_s$ ) and finish ( $T_f$ ) temperatures, mass loss contribution of the single degradation step and total mass loss reached after the step registered by TGA analysis of R7 resin in  $N_2$  atmosphere

R7 $N_2$ event #	$T_s$ /°C	$T_f$ /°C	Event mass loss /%	Total mass loss /%
1	160.6	248.5	2.1	2.1
2	255.4	321.1	4.6	6.7
3	321.2	334.9	1.9	8.6
4	335.5	449.3	21.8	30.4
5	451.4	1050	26.8	57.2

**Table 14** Degradation step start ( $T_s$ ) and finish ( $T_f$ ) temperatures, mass loss contribution of the single degradation step and total mass loss reached after the step registered by TGA analysis of Ph resin in air atmosphere

Ph Air event #	$T_s$ /°C	$T_f$ /°C	Event mass loss /%	Total mass loss /%
1	40.7	124.2	1.0	1.0
2	140.3	158.1	1.4	2.4
3	161.6	257.2	2.3	4.7
4	273.8	690.0	95.3	100.0

**Table 15** Degradation step start ( $T_s$ ) and finish ( $T_f$ ) temperatures, mass loss contribution of the single degradation step and total mass loss reached after the step registered by TGA analysis of R6 resin in air atmosphere

R6 Air event #	$T_s$ /°C	$T_f$ /°C	Event mass loss /%	Total mass loss /%
1	150.7	252.9	3.1	3.1
2	256.2	445.9	29.0	32.1
3	450.0	521.4	13.5	45.6
4	525.9	711.2	53.4	99.0

single event and the total mass loss reached) are reported in Tables 14–16.

Similarly to the considerations made for the  $N_2$  atmosphere TGA, some of the degradation events in air atmosphere were overlapping with other concurring steps, and thus their contributions were not unequivocally distinguishable. In the air atmosphere case, Ph event 4, R6 events 1, 2 and 3 and R7 events 1, 2, 3 and 4 show overlapping contributions between each other or with other background events.

TGA carried out in air atmosphere reach the maximum mass loss well before the end of the test, and the mass

**Table 16** Degradation step start ( $T_s$ ) and finish ( $T_f$ ) temperatures, mass loss contribution of the single degradation step and total mass loss reached after the step registered by TGA analysis of R7 resin in air atmosphere

R7 Air event #	$T_s$ /°C	$T_f$ /°C	Event mass loss /%	Total mass loss /%
1	148.7	257.3	2.6	2.6
2	260.3	410.5	16.4	19.0
3	411.3	433.9	3.7	22.7
4	435.4	521.4	17.3	40.0
5	525.1	728.9	48.9	98.9

residue is always minimal. Ph shows no mass residue, while R6 and R7 present around 1% final char mass residue.

**Author Contributions** DC: conceptualization, methodology, experimental work, formal analysis, writing—original draft preparation, main revision. CM: experimental work, resources, writing—review and editing, supervising during revision. GS: supervision, resources, writing—review and editing. LF: conceptualization, methodology, supervision, writing—review and editing, revision work. All authors have read and agreed to the published version of the manuscript.

**Funding** Open access funding provided by Università degli Studi di Trento within the CRUI-CARE Agreement.

## Declarations

**Conflict of interest** The author(s) certify that they have No Conflict of Interest in the subject matter or materials discussed in this manuscript. We certify that the article is the Authors' original work. The article has not received prior publication and is not under consideration for publication elsewhere. On behalf of all Co-Authors, the corresponding Author shall bear full responsibility for the submission. This research has not been submitted for publication nor has it been published in whole or in part elsewhere. We attest to the fact that all authors listed on the title page have contributed significantly to the work, have read the manuscript, attest to the validity and legitimacy of the data and its interpretation.

**Open Access** This article is licensed under a Creative Commons Attribution 4.0 International License, which permits use, sharing, adaptation, distribution and reproduction in any medium or format, as long as you give appropriate credit to the original author(s) and the source, provide a link to the Creative Commons licence, and indicate if changes were made. The images or other third party material in this article are included in the article's Creative Commons licence, unless indicated otherwise in a credit line to the material. If material is not included in the article's Creative Commons licence and your intended use is not permitted by statutory regulation or exceeds the permitted use, you will need to obtain permission directly from the copyright holder. To view a copy of this licence, visit <http://creativecommons.org/licenses/by/4.0/>.

## References

- Eriksson M, Jacobson S. Tribological surfaces of organic brake pads. *Tribol Int.* 2000;33:817–27. [https://doi.org/10.1016/S0301-679X\(00\)00127-4](https://doi.org/10.1016/S0301-679X(00)00127-4).
- Dante RC. Binders and organic materials. In: *Handbook of friction materials and their applications*, Elsevier; 2016, pp. 135–53. <http://dx.doi.org/https://doi.org/10.1016/B978-0-08-100619-1.00010-9>
- Rajan BS, Balaji MAS, Sathickbasha K, Hariharasakthisudan P. Influence of binder on thermomechanical and tribological performance in brake pad. *Tribol Ind.* 2018;40:654–69. <https://doi.org/10.24874/ti.2018.40.04.12>.
- Joo BS, Chang YH, Seo HJ, Jang H. Effects of binder resin on tribological properties and particle emission of brake linings. *Wear.* 2019;434–435:202995. <https://doi.org/10.1016/j.wear.2019.202995>.
- Aleman M, et al. Dry sliding of a low steel friction material against cast iron at different loads: characterization of the friction layer and wear debris. *Wear.* 2017;376–377:1450–9. <https://doi.org/10.1016/j.wear.2017.01.040>.
- Aleman M, Wahlström J, Olofsson U. On the influence of car brake system parameters on particulate matter emissions. *Wear.* 2018;396–397:67–74. <https://doi.org/10.1016/j.wear.2017.11.011>.
- Aleman M, Nosko O, Metinoz I, Olofsson U. A study on emission of airborne wear particles from car brake friction pairs. *SAE Int J Mater Manf.* 2015;9:147–57. <https://doi.org/10.4271/2015-01-2665>.
- Gupta MK, Hindersinn RR. Shelf life of phenolic resole resins. *Polym Eng Sci.* 1987;27:976–8. <https://doi.org/10.1002/polb.760271308>.
- Pizzi A, Ibeh CC. 2 - Phenol-Formaldehydes. In: Dodiuk H, Goodman SH., editors. *Handbook of Thermoset Plastics*, 3rd ed. William Andrew Publishing; 2014. pp. 13–44.
- Dante RC. Production processes for organic brake pads. In: *Handbook of Friction Materials and their Applications*, Elsevier; 2016, pp. 55–65. doi: <https://doi.org/10.1016/B978-0-08-100619-1.00004-3>.
- Holly FW, Cope AC. Condensation products of aldehydes and ketones with o-aminobenzyl alcohol and o-hydroxybenzylamine. *J Am Chem Soc.* 1944;66:1875–9. <https://doi.org/10.1021/ja01239a022>.
- Yang P, Gu Y. A novel benzimidazole moiety-containing benzoxazine: synthesis, polymerization, and thermal properties. *J Polym Sci A Polym Chem.* 2012;50:1261–71. <https://doi.org/10.1002/pola.25873>.
- Liu Y, Zhang H, Wang M, Liao C, Zhang J. Thermal degradation behavior and mechanism of polybenzoxazine based on bisphenol-S and methylamine. *J Therm Anal Calorim.* 2013;112:1213–9. <https://doi.org/10.1007/s10973-012-2678-7>.
- Yang P, Wang X, Fan H, Gu Y. Effect of hydrogen bonds on the modulus of bulk polybenzoxazines in the glassy state. *Phys Chem Chem Phys.* 2013;15:15333. <https://doi.org/10.1039/c3cp51001h>.
- Yang P, Gu Y. Synthesis of a novel benzoxazine-containing benzoxazole structure and its high performance thermoset. *J Appl Polym Sci.* 2012;124:2415–22. <https://doi.org/10.1002/app.35305>.
- Chirachanchai S, Phongtamrug S, Laobuthee A, Tashiro K. Mono-Substituted Phenol-Based Benzoxazines. In: *Handbook of Benzoxazine Resins*, Elsevier; 2011, pp. 111–26. doi: <https://doi.org/10.1016/B978-0-444-53790-4.00049-7>.
- Wirasate S, Dhumrongvaraporn S, Allen DJ, Ishida H. Molecular origin of unusual physical and mechanical properties in novel phenolic materials based on benzoxazine chemistry. *J Appl Polym Sci.* 1998;70:1299–306. [https://doi.org/10.1002/\(SICI\)1097-4628\(19981114\)70:7%3c1299::AID-APP6%3e3.0.CO;2-H](https://doi.org/10.1002/(SICI)1097-4628(19981114)70:7%3c1299::AID-APP6%3e3.0.CO;2-H).
- Ishida H, Nakamura M. Mechanical and thermal properties of new crosslinkable telechelics with benzoxazine moiety at the chain end. *Polymer.* 2009;50:2688–95.

19. Bandeira CF, Pereira AC, Botelho EC, Costa ML. Benzoxazine resin and their nanostructured composites cure kinetic by DSC. *J Mater Res.* 2013;28:6.
20. Gu Y, Li M. Molecular modeling. In *Handbook of Benzoxazine Resins*, Elsevier; 2011, pp. 103–10. doi: <https://doi.org/10.1016/B978-0-444-53790-4.00048-5>.
21. Endo T, Sudo A. Chapter 3 - molecular designs of benzoxazines with enhanced reactivity based on utilization of neighboring-group participation and introduction of thioether moiety. In Ishida H, Froimowicz P., editors. *Advanced and emerging polybenzoxazine science and technology*, Elsevier; 2017, pp. 23–33. doi: <https://doi.org/10.1016/B978-0-12-804170-3.00003-2>.
22. Zeng K, Huang J, Ren J, Ran Q. Curing reaction of benzoxazine under high pressure and the effect on thermal resistance of polybenzoxazine. *Macromol Chem Phys.* 2019;220:1800340. <https://doi.org/10.1002/macp.201800340>.
23. Pei L, et al. Preparation of low temperature cure polybenzoxazine coating with enhanced thermal stability and mechanical properties by combustion synthesis approach. *Polymer.* 2021;220:123573. <https://doi.org/10.1016/j.polymer.2021.123573>.
24. Ran Q, Gu Y, Ishida H. Thermal degradation mechanism of polybenzoxazines. In: *Advanced and emerging polybenzoxazine science and technology*, Elsevier; 2017, pp. 171–04. doi: <https://doi.org/10.1016/B978-0-12-804170-3.00011-1>.
25. Verge P. Symmetric versus asymmetric di-Bz monomer design: structure-to-properties relationship. In: *Advanced and emerging polybenzoxazine science and technology*; 2017, pp. 87–107. <https://doi.org/10.1016/B978-0-12-804170-3.00007-X>
26. Zhang K, Froimowicz P, Ishida H. Development of new generation benzoxazine thermosets based on smart ortho-benzoxazine chemistry. In: *Advanced and emerging polybenzoxazine science and technology*, Elsevier; 2017, pp. 35–64. doi: <https://doi.org/10.1016/B978-0-12-804170-3.00004-4>.
27. Lu Y, Yu X, Han L, Zhang K. Recent progress of high performance thermosets based on norbornene functional benzoxazine resins. *Polymers.* 2021;13:1417. <https://doi.org/10.3390/polym13091417>.
28. Bai Y, Yang P, Zhang S, Li Y, Gu Y. Curing kinetics of phenolphthalein–aniline-based benzoxazine investigated by non-isothermal differential scanning calorimetry. *J Therm Anal Calorim.* 2015;120:1755–64. <https://doi.org/10.1007/s10973-015-4544-x>.
29. Wang P, Liu M, Ran Q. The study on curing and weight-loss mechanisms of benzoxazine during thermal curing process. *Polymer Degrad Stab.* 2020;179:109279. <https://doi.org/10.1016/j.polymerdegradstab.2020.109279>.
30. Shen SB, Ishida H. Development and characterization of high-performance polybenzoxazine composites. *Polym Compos.* 1996;17:710–9. <https://doi.org/10.1002/pc.10663>.
31. Menapace C, Leonardi M, Secchi M, Bonfanti A, Gialanella S, Straffelini G. Thermal behavior of a phenolic resin for brake pad manufacturing. *J Therm Anal Calorim.* 2019;137:759–66. <https://doi.org/10.1007/s10973-019-08004-2>.
32. Ramdani N, Derradji M, Mokhnache EO. Natural fiber reinforced polybenzoxazine composites: a review. *Mater Today Commun.* 2022;31:103645. <https://doi.org/10.1016/j.mtcomm.2022.103645>.
33. Bessa W, Tarchoun AF, Trache D, Derradji M. Preparation of amino-functionalized microcrystalline cellulose from Arundo Donax L. and its effect on the curing behavior of bisphenol A-based benzoxazine. *Thermochim Acta.* 2021;698:178882. <https://doi.org/10.1016/j.tca.2021.178882>.
34. Gurunath PV, Bijwe J. Potential exploration of novel green resins as binders for NAO friction composites in severe operating conditions. *Wear.* 2009;267:789–96. <https://doi.org/10.1016/j.wear.2009.02.012>.
35. Leonardi M, Menapace C, Matějka V, Gialanella S, Straffelini G. Pin-on-disc investigation on copper-free friction materials dry sliding against cast iron. *Tribol Int.* 2018;119:73–81. <https://doi.org/10.1016/j.triboint.2017.10.037>.
36. Menapace C, Leonardi M, Matějka V, Gialanella S, Straffelini G. Dry sliding behavior and friction layer formation in copper-free barite containing friction materials. *Wear.* 2018;398–399:191–200. <https://doi.org/10.1016/j.wear.2017.12.008>.
37. Leonardi M, Alemanni M, Straffelini G, Gialanella S. A pin-on-disc study on the dry sliding behavior of a Cu-free friction material containing different types of natural graphite. *Wear.* 2020;442–443:203157. <https://doi.org/10.1016/j.wear.2019.203157>.
38. Turi EA. *Thermal characterization of polymeric materials.* vol. 52. Academic Press, Inc.; 1982. <https://doi.org/10.1177/004051758205200819>
39. Kimura H, Matsumoto A, Hasegawa K, Fukuda A. New thermosetting resin from bisphenol A-based benzoxazine and bisoxazoline. *J Appl Polym Sci.* 1999;72:1551–8. [https://doi.org/10.1002/\(SICI\)1097-4628\(19990620\)72:12%3c1551::AID-APP7%3e3.0.CO;2-5](https://doi.org/10.1002/(SICI)1097-4628(19990620)72:12%3c1551::AID-APP7%3e3.0.CO;2-5).
40. Wang X, Chen F, Gu Y. Influence of electronic effects from bridging groups on synthetic reaction and thermally activated polymerization of bisphenol-based benzoxazines: influence of electronic effects. *J Polym Sci A Polym Chem.* 2011;49:1443–52. <https://doi.org/10.1002/pola.24566>.
41. Gaina C, Ursache O, Gaina V, Musteata V-E. High performance thermosets based on multifunctional intermediates containing allyl, maleimide and benzoxazine groups. *J Polymer Res.* 2013;20:263. <https://doi.org/10.1007/s10965-013-0263-9>.
42. García-Martínez V, Gude MR, Ureña A. Understanding the curing kinetics and rheological behaviour of a new benzoxazine resin for carbon fibre composites. *React Funct Polymers.* 2018;129:103–10. <https://doi.org/10.1016/j.reactfunctpolym.2017.02.005>.
43. Bandeira CF, Costa ACAD, Montoro SR, Costa ML, Botelho EC. Thermal behavior evaluation of benzoxazine reinforced with MACADAMIA biomass composites. *J Appl Polymer Sci.* 2022;139:52160. <https://doi.org/10.1002/app.52160>.
44. Feng Z, et al. A novel bio-based benzoxazine resin with outstanding thermal and superhigh-frequency dielectric properties. *J Mater Sci Mater Electron.* 2020;31:4364–76. <https://doi.org/10.1007/s10854-020-02995-7>.
45. Vyazovkin S, Burnham AK, Criado JM, Pérez-Maqueda LA, Popescu C, Sbirrazzuoli N. ICTAC Kinetics Committee recommendations for performing kinetic computations on thermal analysis data. *Thermochim Acta.* 2011;520:1–19. <https://doi.org/10.1016/j.tca.2011.03.034>.
46. Vyazovkin S. Modern isoconversional kinetics: from misconceptions to advances. In: *Handbook of thermal analysis and calorimetry*; 2018, pp. 131–72. doi: <https://doi.org/10.1016/B978-0-444-64062-8.00008-5>.
47. Akahira T, Sunose T. Method of determining activation deterioration constant of electrical insulating materials. *Res Rep Chiba Inst Technol Sci Technol.* 1971;16:22–31.
48. Vyazovkin S. Kissinger method in kinetics of materials: things to beware and be aware of. *Molecules.* 2020;25:2813. <https://doi.org/10.3390/molecules25122813>.
49. Grigoratos T et al. Statistical assessment and temperature study from the interlaboratory application of the WLTP–brake cycle; 2020. p. 22.
50. Agudelo C. Thermal regimes during proving ground measurements using WLTP-Brake cycle, In: *United nations particle measurement programme informal working group (UNECE PMP IWG)*; 2018.
51. Ishida H, Sanders DP. Regioselectivity and network structure of difunctional alkyl-substituted aromatic amine-based polybenzoxazines. *Macromolecules.* 2000;33:8149–57. <https://doi.org/10.1021/ma991836t>.

52. Wang MW, Jeng RJ, Lin CH. Study on the ring-opening polymerization of benzoxazine through multisubstituted polybenzoxazine precursors. *Macromolecules*. 2015;48:530–5. <https://doi.org/10.1021/ma502336j>.
53. Wang Y-X, Ishida H. Synthesis and properties of new thermoplastic polymers from substituted 3,4-Dihydro-2H-1,3-benzoxazines. *Macromolecules*. 2000;33:2839–47. <https://doi.org/10.1021/ma9909096>.
54. Aohikari V. Thermal decomposition of vermiculites: kinetics of dehydration and dehydroxylation processe, vol. 42; 1983. p. 5.
55. Barlow SG, Manning DAC. Influence of time and temperature on reactions and transformations of muscovite mica. *Br Ceram Trans*. 1999;98:5.
56. Ingo GM, D'Uffizi M, Falso G, Bultrini G, Padeletti G. Thermal and microchemical investigation of automotive brake pad wear residues. *Thermochim Acta*. 2004;418:61–8. <https://doi.org/10.1016/j.tca.2003.11.042>.
57. Ramousse S, Høj JW, Sørensen OT. Thermal characterisation of brake pads. *J Therm Anal Calorim*. 2001;64:933–43. <https://doi.org/10.1023/A:1011575013779>.
58. Verma PC, Ciudin R, Bonfanti A, Aswath P, Straffelini G, Gialanella S. Role of the friction layer in the high-temperature pin-on-disc study of a brake material. *Wear*. 2016;346–347:56–65. <https://doi.org/10.1016/j.wear.2015.11.004>.
59. Bijwe J, Nidhi NM, Satapathy BK. Influence of modified phenolic resins on the fade and recovery behavior of friction materials. *Wear*. 2005;259:1068–78. <https://doi.org/10.1016/j.wear.2005.01.011>.
60. Österle W, Urban I. Third body formation on brake pads and rotors. *Tribol Int*. 2006;39:401–8.
61. Eriksson M, Bergman F, Jacobson S. On the nature of tribological contact in automotive brakes. *Wear*. 2002;252:26–36.
62. Ria T, Soib M, Kasir R. Selection of best formulation for semi-metallic brake friction materials development, In: Kondoh K., editor. *Powder metallurgy*; 2012. doi: <https://doi.org/10.5772/33909>
63. Mittemeijer EJ. Analysis of the kinetics of phase transformations. *J Mater Sci*. 1992;27:3977–87. <https://doi.org/10.1007/BF01105093>.

**Publisher's Note** Springer Nature remains neutral with regard to jurisdictional claims in published maps and institutional affiliations.